J. Fluid Mech. (2002), *vol.* 460, *pp.* 349–380. © 2002 Cambridge University Press
DOI: 10.1017/S0022112002008364 Printed in the United Kingdom

Coherent structure in the turbulent planar jet. Part 2. Structural topology via POD eigenmode projection

By S. V. GORDEYEV AND F. O. THOMAS

Hessert Center for Aerospace Research, Department of Aerospace and Mechanical Engineering, University of Notre Dame, Notre Dame, IN 46556, USA

(Received 5 March 2001 and in revised form 14 December 2001)

The topology of the large-scale structure in the similarity region of a turbulent planar jet is investigated experimentally. The large-scale structure is reconstructed in physical space by projection of measured proper orthogonal decomposition eigenmodes onto instantaneous flow-field realizations. The instantaneous flow-field realizations are obtained by a spanwise aligned triple X-wire rake arrangement which is used in conjunction with the linear stochastic estimation technique. Instantaneous realizations are also acquired via a second triple rake arrangement which provides an assessment of the effect of spatial aliasing on the resulting structural topology. Results indicate that the self-similar large-scale structure in the planar jet consists of a dominant planar component consisting of two lines of large-scale spanwise vortices arranged approximately asymmetrically with respect to the jet centreline. This planar component of the structure resembles the classic Kármán vortex street. There is a strong interaction between structures on opposite sides of the jet in the form of nearly two-dimensional lateral streaming motions that extend well across the flow. In addition, results indicate that the effect of the nonplanar spanwise modes is to both tilt and bend the primary spanwise vortex tubes and thereby redistribute large-scale vorticity. The bending occurs primarily in the streamwise direction. The degree to which the spanwise vortices are distorted varies greatly; in some cases they are nearly streamwise oriented and in others only slight distortion of a spanwise vortex is noted. Based upon the experimental results, prospects for low-order modelling of the jet large-scale structure are discussed.

1. Introduction

1.1. *Background, motivation and objectives*

Previous studies of the planar turbulent jet have suggested the presence of large-scale organized motions in the similarity region. By large-scale we mean spatial scales of the order of the local jet half-width. These studies were described in Part 1 (Gordeyev & Thomas 2000) and in the review by Thomas (1991). While they leave little doubt regarding the existence of large-scale organized motions in the similarity region of the planar turbulent jet, questions regarding the origin, topology and dynamics remain. Indeed, our current understanding of the jet's large-scale structure topology is embodied in the sketch shown in figure 13 of Mumford (1982) and in the conditioned velocity vector field shown in figure 6 of Antonia *et al.* (1986). It is a primary objective of this paper to provide a more detailed description of the

https://doi.org/10.1017/S0022112002008364 Published online by Cambridge University Press

structural topology responsible for large-scale motions in the planar turbulent jet. This is a prerequisite to the longer-term goal of providing a low-order dynamical system-based model of these motions.

In Part 1, we applied the proper orthogonal decomposition (POD) to investigate the average large-scale structure in the similarity region of a turbulent planar jet. In recognition of the fact that there is no universally accepted definition of the term 'large-scale structure', we chose to consider a summation of the dominant POD modes (including the mean flow) as synonymous with this term. This has the advantage of representing the largest scales of motion within a mathematical framework that facilitates modelling their dynamics. Using twin cross-stream rakes of X-wire probes separated in the spanwise direction, the POD eigenfunctions and associated eigenvalues were extracted and a rapid convergence of the eigenvalues documented. When scaled appropriately, the POD eigenmodes and associated eigenvalues were found to exhibit self-similarity. This result is consistent with earlier theoretical work by Ewing (1995) which indicated that the equation for the propagation of the correlation tensor in the planar jet admits to self-similar solutions. Since the average large-scale structure may be represented as a summation of POD modes, their self-similarity represents a sufficient condition for the self-similarity of the structure itself.

In that implementation of the POD, the flow was considered stationary in time and the spanwise coordinate was treated as homogeneous. The cross-flow direction was taken as the single inhomogeneous coordinate. The resulting streamwise, lateral and spanwise component POD eigenmodes $\varphi_{\alpha}^{(n)}(y, St, k_z)$ were obtained in a mixed physical–Fourier space where y denotes the cross-stream spatial coordinate, St is a Strouhal number based on the local mean velocity half-with $b(x)$ and the local jet centreline mean velocity U_m and k_z is the spanwise wavenumber. Superscript n denotes mode number and subscript α the component. The associated eigenvalue distributions in (k_z, St)-space were also obtained.

Since the planar jet POD eigenfunctions presented in Part 1 are determined in a mixed physical–Fourier space, their reconstruction in the physical domain is required to more readily interpret the topology of the flow structure and to capture its dynamics. As pointed out by Lumley (1967, 1970), POD eigenfunctions are known only to within an arbitrary function of phase along homogeneous directions. The phase information required for reconstruction of the large-scale structure in physical space is obtained by projection of the POD modes back onto instantaneous realizations of the flow field.

In this paper, the POD eigenfunctions obtained experimentally in the similarity region of the turbulent planar jet, as described in Part 1, are used in conjunction with a triple X-wire rake arrangement in order to reconstruct the large-scale structure in physical space and examine its temporal behaviour. In order to perform the projection, two approaches are used. In the first, we use a version of the complementary technique developed by Bonnet *et al.* (1994). As will be described in detail, this method uses linear stochastic estimation (LSE) to generate the instantaneous flow-field realizations required for POD eigenfunction projection. The application of LSE requires fewer probes to be placed in the inhomogeneous coordinate so that more can be placed in the spanwise direction. This is particularly important for examining the spanwise variation of the structure with a minimal level of spatial aliasing. A second projection method is performed in support of the first and allows for an independent determination of the planar portion of the structure. Comparison of the planar parts resulting from both projection methods provides an assessment of the effect of both spatial aliasing and the LSE interpolation on the resulting large-scale structure. Using

https://doi.org/10.1017/S0022112002008364 Published online by Cambridge University Press

these methods, the jet coherent structure is reconstructed in physical space and its essential topology documented. Comparisons are made with previously published interpretations regarding the planar jet structural topology and the prospects for constructing a dynamical system-based model are also addressed.

The remainder of the paper is organized as follows. In § 2, we briefly describe the flow-field facility and measurement apparatus. For completeness, the method by which the POD spatial eigenmodes were extracted and their basic character are also reviewed in § 2. The procedures by which we use the triple X-wire rake and LSE for the projection of these modes onto instantaneous realizations of the flow is the subject of § 3. The resulting turbulent planar jet large-scale structure is described in § 4. The results of the study are summarized and prospects for dynamical system modelling are discussed in § 5.

2. Description of the experiment

2.1. *Experimental facility and instrumentation*

All the experiments were conducted in the planar jet flow-field facility located at the Hessert Center for Aerospace Research at the University of Notre Dame. The experimental set-up was described in detail in Part 1 and by Gordeyev (1999). The jet is formed by a two-dimensional nozzle that has a contraction ratio of 16 : 1 and ends in a two-dimensional slot that is $D = 1.27\,\mathrm{cm}$ in width and $H = 45.7\,\mathrm{cm}$ in height giving an aspect ratio (height/width) of 36 : 1. The flow field is formed between two horizontal confining plates of dimension 2.5 m in the flow direction and 1.61 m in width which serve to keep the base flow two-dimensional in nature. In this paper, x will denote the streamwise spatial coordinate which is made non-dimensional by the nozzle slot width, D. The cross-stream spatial coordinate is y and is made non-dimensional by the local mean velocity half-width, $b(x)$. The spanwise spatial coordinate extending in the direction of mean flow homogeneity is denoted by z. The origin of the z-axis is chosen in the centreplane midway between the two flow-field confining plates. The fluctuating velocity components corresponding to coordinates x, y, z are denoted by u, v, w, respectively.

For the experiments reported, the nozzle exit velocity was $U_0 = 35\,\mathrm{m\,s^{-1}}$ which corresponds to a Reynolds number (based on nozzle slot width) of $Re_D = 28000$. The initial jet mean velocity profiles are flat (i.e. a 'top-hat' shape) with the mean velocity variation across the nascent jet shear layers closely approximated by a classic hyperbolic tangent type of profile. The jet potential core is engulfed by the widening jet shear layers by $x/D \approx 4$ and self-similarity of the mean velocity profiles occurs for $x/D > 10$. Mean flow widening and velocity decay rates were reported in Part 1 and show good agreement with previously published values. Second-order turbulence moments (also presented in Part 1) exhibit similarity for $x/D > 50$. Since the focus of this work concerns the nature of large-scale motions in the similarity region, the POD measurements were performed over the streamwise interval $50 \leqslant x/D \leqslant 90$. Although the jet facility allows measurements to be made at larger x/D, the low velocities associated with these stations give rise to larger relative uncertainties in the multi-component hot-wire measurements. This streamwise range quoted above represents an optimum in the sense of achieving both the desired self-similar jet behaviour and minimal measurement uncertainty.

Rakes of X-wire probes operated in the constant temperature mode were used to measure the fluctuating velocity in the jet. Each rake uses miniature X-wire probes

https://doi.org/10.1017/S0022112002008364 Published online by Cambridge University Press

fabricated by Auspex Corporation (types A55P61 or AHWX-100). Three rakes of eight X-wires each were used. The hot-wire calibration procedure is described in Part 1. The required 48-channels of constant temperature hot-wire anemometry and associated anti-alias filters were fabricated in-house. The dynamic response of the transducers was found to be flat to 50 kHz, which was more than sufficient for the needs of the experiments. The anti-alias filtered output voltages from the hot wires were simultaneously sampled and digitized by means of a 64-channel MSXB data acquisition system made by MicroStar Laboratories. This system is capable of simultaneously sampling the 48 hot-wire anemometer output voltages at rates up to 33.3 kHz with no detectable phase lag between channels. Digital data were logged to an external drive in binary format and pre-processed on a laboratory PC. The data were subsequently uploaded to a Sun SPARCstation for post-processing.

2.2. *Extraction of the POD modes and associated eigenvalues*

In this section, the method by which the POD spatial eigenmodes and associated eigenvalues were extracted is described briefly and some key results presented. Since this was the focus of Part 1, only those aspects considered essential for providing the relevant framework for the current work are described here.

Cross-spectral measurements involving all three fluctuating velocity components at selected x/D planes in the similarity region of the jet ($50 \leqslant x/D \leqslant 90$) were performed by means of two spanwise-separated rakes of eight X-wire probes each. Both of the rakes were at the same x/D location and were oriented in the cross-stream direction, parallel to each other. The two rakes were separated in the spanwise direction by a user selected distance $z - z' = \Delta z$. Using the two-rake system the cross-spectral matrix $S_{\alpha\beta}(y, y', f, \Delta z)$ was computed directly from the Fourier transformation of the individual velocity–time histories (see Bendat & Piersol 1986),

$$S_{\alpha\beta}(y, y', f, \Delta z) = \lim_{T\to\infty} \frac{1}{T} \langle \hat{u}^*_\alpha(y, z, f) \hat{u}_\beta(y', z', f) \rangle , \tag{2.1}$$

where $\langle\cdot\rangle$ denotes an ensemble average and Greek subscripts denote a fluctuating velocity component u, v or w. The velocity measurement $u_\alpha(y, z, t)$ corresponds to the first rake and $u_\beta(y', z', t')$ corresponds to the second. Note that the X-wire probes are capable of the simultaneous measurement of either ($\alpha = u, \beta = v$) or ($\alpha = u, \beta = w$) depending on their orientation in the flow field. The quantity $\hat{u}_\alpha(y, z, f) \equiv \int_0^T u_\alpha(y, z, t) \exp(-2\pi i f t) \mathrm{d}t$ denotes the temporal Fourier transformation of the velocity vector for each block, T is the total time duration of the data block and the asterisk denotes a complex conjugate. A spatial Fourier transformation in the homogeneous z-direction provides a spanwise wavenumber-dependent cross-spectral matrix,

$$\Phi_{\alpha\beta}(y, y'; f, k_z) = \int S_{\alpha\beta}(y, y'; f, \Delta z)\, \mathrm{e}^{-\mathrm{i}k_z \Delta z} \mathrm{d}(\Delta z), \tag{2.2}$$

where k_z is a spanwise wavenumber. The matrix $\Phi_{\alpha\beta}(y, y'; f, k_z)$ essentially unfolds $S_{\alpha\beta}(y, y'; f, \Delta z)$ in spanwise wavenumber space.

As shown in Lumley (1970), the spectral correlation tensor $\Phi_{\alpha\beta}(y, y'; f, k_z)$ will be a kernel in the integral equation to find the POD modes for different frequencies f, and spanwise wavenumbers, k_z,

$$\int \Phi_{\alpha\beta}(y, y'; f, k_z) \varphi^{(n)}_\beta(y'; f, k_z)\, \mathrm{d}y' = \lambda^{(n)}(f, k_z) \varphi^{(n)}_\alpha(y; f, k_z). \tag{2.3}$$

Here superscript n denotes mode number. The solution of (2.3) gives a complete set

https://doi.org/10.1017/S0022112002008364 Published online by Cambridge University Press

of orthonormal eigenfunctions $\varphi_\alpha^{(n)}(y;f,k_z)$ with corresponding positive eigenvalues $\lambda^{(n)}(f,k_z)$.

In order to reconstruct the POD modes in physical space, all components of the $\Phi_{\alpha\beta}$-matrix must be given. Unfortunately, the term Φ_{wv} cannot be measured directly using the X-wire rakes. It can be obtained, however, from mass conservation requirements using a procedure described in Ukeiley & Glauser (1995) and Ukeiley *et al.* (2001). A Fourier transform of the continuity equation gives,

$$\frac{\partial \hat{u}_\alpha(y,z,f)}{\partial x_\alpha} = \frac{\partial \hat{u}(y,z,f)}{\partial x} + \frac{\partial \widehat{v}(y,z,f)}{\partial y} + \frac{\partial \widehat{w}(y,z,f)}{\partial z} = 0. \tag{2.4}$$

Since the spreading rate of the jet is small, $\mathrm{d}b/\mathrm{d}x \approx 0.1$, the streamwise direction is weakly inhomogeneous and, as a first approximation, can be considered homogeneous. In addition, according to measurements by Thomas & Brehob (1986), the structures in the self-similar region of the turbulent planar jet convect at approximately 60% of the local jet centreline mean velocity ($U_c \approx 0.6U_m$). We form the complex conjugate of equation (2.4), multiply by $\widehat{v}(y',z',f)$ and average over multiple ensembles. After performing a spatial Fourier transform in the z-direction and applying a constant group speed hypothesis in the x-direction,

$$\frac{\partial}{\partial x} = -\frac{1}{U_c}\frac{\partial}{\partial t} = -2\pi \mathrm{i} f \frac{1}{U_c} = \mathrm{i}k_x, \tag{2.5}$$

equation (2.4) can be rewritten in terms of $\Phi_{\alpha v}$ (2.2) as,

$$\mathrm{i}k_x \Phi_{uv} + \frac{\partial \Phi_{vv}}{\partial y} + \mathrm{i}k_z \Phi_{wv} = 0. \tag{2.6}$$

From the above relation, Φ_{wv} can be easily calculated. The remaining terms Φ_{vu}, Φ_{wu} and Φ_{vw} can be found using the property that the Φ-matrix is Hermitian,

$$\Phi_{\alpha\beta}(y,y';k_x,k_z) = \Phi^*_{\beta\alpha}(y',y;k_x,k_z). \tag{2.7}$$

As described at length in Part 1, by exploiting symmetries of the $\Phi_{\alpha\beta}$ matrix and by application of a finite quadrature form of (2.3), the POD eigenfunctions $\varphi_\alpha^{(n)}(y_i;f,k_z)$ and associated eigenvalues $\lambda^{(n)}(f,k_z)$ were experimentally determined. Part 1 contains an extensive discussion of sampling issues related to the avoidance of spatial and temporal aliasing in this process. A more general treatment of sampling issues related to multi-point hot-wire measurements in turbulent flows is presented in Glauser & George (1992).

With suitable scaling by global flow-field variables, the planar jet POD eigenvalues and eigenfunctions were shown to exhibit self-similar behaviour. It was also shown that the flow supports a structure which has a dominant planar component which is aligned in the spanwise direction ($k_z = 0$) as well as an essentially three-dimensional part with asymmetrical mean shape in the y-direction. As such, both planar and non-planar POD modes will be used in this paper in order to restore and characterize the shape of the jet large-scale structure in physical space.

It was demonstrated in Part 1 that the energy content of the POD modes, as expressed through their respective eigenvalues, show rapid convergence with mode number. For example, the v-component POD mode converges particularly rapidly with 61% of the v-fluctuation energy contained in mode 1 while the first three modes capture nearly 90% of $\overline{v^2}$. The energy convergence of the u- and w-component modes is less rapid, but still the first four modes each contain 85% and 80% of their respective fluctuation energies.

https://doi.org/10.1017/S0022112002008364 Published online by Cambridge University Press

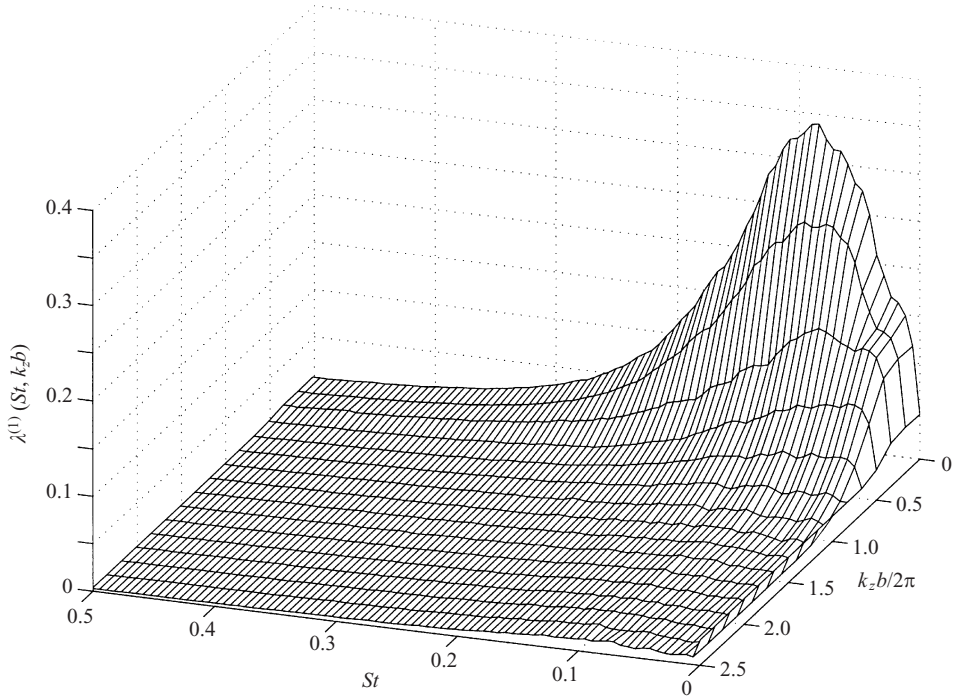


FIGURE 1. Measured mode 1 eigenvalues $\lambda^{(1)}(St, k_z b)$ at $x/D = 70$.

The planar POD eigenmodes based upon the full $\Phi_{\alpha\beta}$ matrix are in general agreement with those presented in figures 21 and 23 of Part 1 which are based only on the cross-spectral matrix terms Φ_{uu}, Φ_{vv} and Φ_{uv} (i.e. with the w-component completely neglected). The first POD mode eigenvalue distribution, $\lambda^{(1)}(St, k_z)$, as obtained at $x/D = 70$ is presented in figure 1. The result may be considered representative of those obtained at other locations in the similarity region. The eigenvalue distribution exhibits a well-defined peak at $St = 0.09$ and $k_z = 0$. There is a gradual roll-off in $\lambda^{(1)}$with spanwise wavenumber and no significant energy content for $k_z b/2\pi > 1$. Similarly, there is little energy for $St > 0.3$. Non-planar POD modes are also quite similar to those presented in Part 1. For $k_z > 0$, the u-component mode is dominant. In comparison to the u-mode, the v-mode amplitude decreases much more rapidly with k_z. While the v-mode amplitude decreases with k_z, the w-mode increases. For the higher wavenumbers, the amplitude of the w-component is comparable with the v-component which is indicative of a three-dimensional time-averaged structure. Examination of higher POD mode numbers reveals that the v-component exhibits a particularly rapid convergence with mode number.

The POD eigenfunctions depend on Strouhal number (temporal frequency), spanwise wavenumber and lateral position in the inhomogeneous direction. Any velocity realization can be represented as a sum of these eigenfunctions,

$$u_\alpha(y, z, t) = \sum_{n=1}^{\infty} \int\int c^{(n)}(k_z, f)\varphi_\alpha^{(n)}(y; f, k_z) \exp(2\pi i f t) \exp(i k_z z)\, \mathrm{d}f\, \mathrm{d}k_z. \tag{2.8}$$

All the phase information necessary for reconstruction of the coherent structure in the physical domain resides in the coefficients $c^{(n)}(k_z, f)$. In order to find them, a

https://doi.org/10.1017/S0022112002008364 Published online by Cambridge University Press

projection of the POD modes back onto instantaneous realizations of the flow is required. In the following section, we describe the basic procedure by which the POD eigenmodes presented above are restored in the physical domain.

3. Reconstruction of the POD modes in physical space

In order to reconstruct the shape of the POD modes in physical space, $\varphi_\alpha^{(n)}(y;f,k_z) \rightarrow \varphi_\alpha^{(n)}(y;t,z)$, an inverse transform in frequency and wavenumber domains must be performed. However, as is easily demonstrated from (2.3), each of the POD modes are known only up to an arbitrary factor of phase, say $\exp(\mathrm{i}\sigma(f,k_z))$. This follows from the fact that the integration in (2.3) is performed in the y-direction with f and k_z as parameters. In general, the POD modes are ambiguous in phase for all homogeneous directions, as described in Lumley (1970). This phase information required for a local reconstruction of the flow structure can be restored by projection of the POD modes onto instantaneous flow-field realizations $u_\alpha(y,z,t)$ obtained at selected streamwise stations, x/D, in the similarity region of the jet. One approach to doing this would be to use a technique similar to that employed by Citriniti & George (2000) in the axisymmetric shear layer. However, in the far field of the planar jet the lateral velocity component cannot be neglected and as a consequence, this method would require a very large array of multi-sensor probes in the plane $x/D = const.$ Instead, the approach to be described in § 3.1 uses the complementary technique developed by Bonnet *et al.* (1994) in which linear stochastic estimation (LSE) provides the required instantaneous flow-field realizations with a much smaller number of probes. In particular, the effective interpolation provided by LSE is used to reduce the required number of X-wire probes in the inhomogeneous cross-stream direction. This allows more probes to be placed in the spanwise direction which is important since we are interested in characterizing the spanwise variation of the large-scale structure. An alternative method of projecting the POD modes is based on flow-field realizations acquired with a different rake arrangement and allows for an independent estimate of the planar part of the structure. This method is performed in support of the first and provides assessments of both the effect of LSE interpolation in the inhomogeneous coordinate and spatial aliasing of spanwise wavenumber modes on the reconstructed planar part of the large-scale structure.

We next outline both methods beginning with the LSE-based technique. The theory behind the projection method as well as some details regarding implementation are described.

3.1. *POD eigenmode projection via LSE-based flow-field realizations*

3.1.1. *Linear stochastic estimation*

The LSE method proposed by Adrian (1977, 1979) estimates a flow field $\boldsymbol{u}(\boldsymbol{x},t)$ conditioned upon knowledge of the flow $\boldsymbol{u}' \equiv \boldsymbol{u}(\boldsymbol{x}',t')$ at some selected points in space and/or time. Adrian proposed expanding the conditional average $\langle \boldsymbol{u} \,|\, \boldsymbol{u}' \rangle$ in a Taylor series about $\boldsymbol{u}' = 0$ as

$$u_i(\boldsymbol{x},t) = \langle u_i(\boldsymbol{x},t) \,|\, \boldsymbol{u}' \rangle = A_{ij}u'_j + N_{ijk}u'_j u'_k + \ldots, \tag{3.1}$$

where repeated subscripts are summed. If we truncate the series at the linear term, we obtain the estimate,

$$\widetilde{u}_i(\boldsymbol{x},t) = A_{ij}u'_j. \tag{3.2}$$

https://doi.org/10.1017/S0022112002008364 Published online by Cambridge University Press

Here, the approximation of $\boldsymbol{u}(\boldsymbol{x},t)$ by linear stochastic estimation is denoted by $\widetilde{\boldsymbol{u}}(\boldsymbol{x},t)$. The unknown coefficient tensor $\boldsymbol{A}$ can be determined by minimizing the mean-square error between the approximation and the conditional average,

$$\langle[\langle u_i \,|\, \boldsymbol{u}'\rangle - A_{ij}u'_j]^2\rangle \rightarrow \min. \tag{3.3}$$

Simple algebra leads to a set of linear algebraic equations for the estimation coefficients A_{ij},

$$\langle u'_j u'_k\rangle A_{ij} = \langle u_i u'_k\rangle. \tag{3.4}$$

Here $\langle u'_j u'_k\rangle = R_{jk}(\boldsymbol{x}',t')$ is the Reynolds stress tensor, $\langle u_i u'_k\rangle = R_{ik}(\boldsymbol{x},\boldsymbol{x}',t,t')$ is the two-point, second-order, space–time velocity correlation. From (3.4), it follows that the linear stochastic estimation exploits the second-order correlation function between the given event data and the flow field at certain selected points. Thus, LSE offers a powerful tool for reconstructing conditionally averaged estimates based on the information from the unconditionally sampled two-point correlation tensor.

When the elements of $\boldsymbol{u}$ and $\boldsymbol{u}'$ are joint normally distributed, the conditional average $\langle \boldsymbol{u} \,|\, \boldsymbol{u}'\rangle$ is a linear function of $\boldsymbol{u}'$ (see Papoulis 1984). Turbulent flows are inherently nonlinear, which leads to non-normal probability distributions. Strictly speaking then, $\langle \boldsymbol{u} \,|\, \boldsymbol{u}'\rangle$ is a nonlinear function of $\boldsymbol{u}'$ for most flows and it would seem that at least some nonlinear terms should be kept in the expansion (3.1). In Adrian (1979), flow structures in isotropic turbulence were investigated using LSE. The accuracy of LSE was evaluated by also including the quadratic term in (3.1). The results of LSE and second-order stochastic estimation were found to be almost identical. In Adrian *et al.* (1989) the validity and accuracy of LSE was investigated in detail by comparing stochastic estimates to conditional averages measured directly in several different turbulent flows. They found that LSE worked well in each of these flows.

Breteton (1982) showed that the result of the stochastic estimation process is strongly dependent upon the event to which the average is conditioned. A series of tests based on one-point velocity measurements in a turbulent boundary layer demonstrated how the stochastic estimation may be refined to give more accurate descriptions of particular coherent motions. It was shown that merely increasing the order of a polynomial model of the event vector would not necessarily increase the accuracy of the stochastic estimation.

For a comprehensive review of the implementation of LSE in turbulent flows, see Adrian (1994).

3.1.2. *Flow-field realizations via a z-aligned triple-rake experiment using LSE*

Instantaneous flow-field realizations required for projection of the POD eigenmodes were obtained via the LSE technique used in conjunction with a triple-rake of X-wire probes. Although measurements were obtained at several streamwise locations over the range $50 \leqslant x/D \leqslant 90$, in this paper we will present only those obtained at $x/D = 70$ which may be considered representative. Below we describe the implementation at the $x/D = 70$ streamwise location. Results will be presented in § 4.

Each rake was oriented in the spanwise z-direction and contained $N_z = 8$ equally spaced X-wire probes. The X-wire probes were oriented so as to simultaneously measure the u and v-component velocity fluctuations. A diagram of the probe rakes in the planar jet flow field is shown in figure 2. The Δz spacing between the probes was chosen as $\Delta z = 0.4b = 3.8\,\mathrm{cm}$. This Δz separation corresponds to a maximum resolved spanwise wavenumber of $k_{z\,\max} = 82.7\,\mathrm{m}^{-1}$ or equivalently, $k_{z\,\max}b/2\pi = 1.25$. It is clear

https://doi.org/10.1017/S0022112002008364 Published online by Cambridge University Press

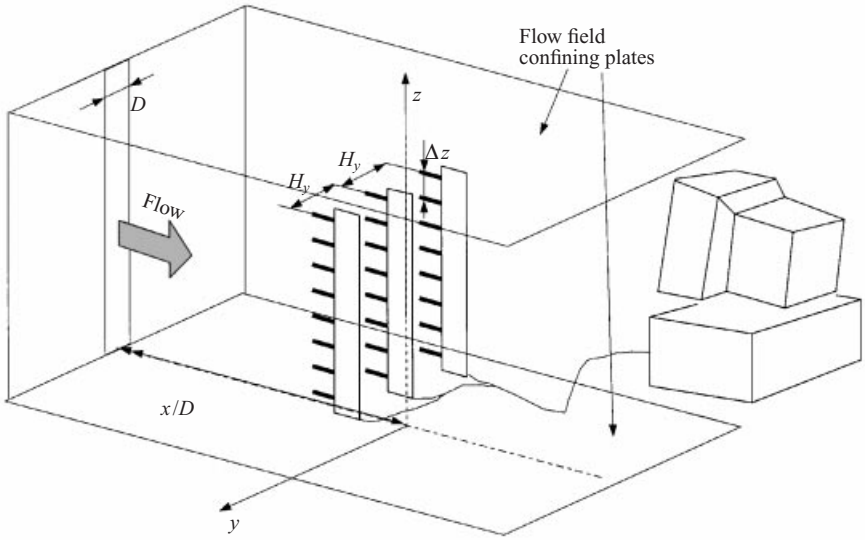


FIGURE 2. The z-aligned triple-rake set-up.

that the instantaneous flow will contain spectral content above this wavenumber so there will be spatial aliasing of higher spanwise wavenumber modes. The key question to be answered is the degree to which the resulting large-scale structural topology is affected by this aliasing of the instantaneous realizations. One straightforward way to address this issue is to perform the projection with larger Δz probe spacing and consequently, with lower $k_{z\,\max}$. By lowering $k_{z\,\max}$, the spatial aliasing will be increased and its effect on the resulting large-scale structural topology can be noted. In effect, this becomes a sensitivity test by which the effect of aliasing on structural topology may be gauged. Later, we will describe a second projection method which is performed with $k_{z\,\max}$ reduced by a factor of 2.5 from the value quoted above. It will be shown that the difference in the planar structural topology resulting from both projection methods is small. This suggests that any spanwise aliasing associated with the probe arrangement is not significant enough to alter the essential conclusions regarding the jet's large-scale topology.

The three rakes were separated in the cross-stream direction by $\Delta y = 5$ cm and were located at $y'/b = -0.4, 0.15$ and 0.7 in order to match the particular y-locations of three of the probes used in the twin-rake experiment reported in Part 1. Some guidance in the lateral positioning of the probes was provided by the turbulent-mixing-layer study by Bonnet *et al.* (1994). This study demonstrated that two probes positioned in the cross-stream direction were sufficient for LSE to capture the instantaneous flow field faithfully. This was one basis for the choice of positioning two of the rakes in the shear layers on opposite sides of the jet and the third near the jet centreline. In order to assess the effect of the limited number of probes in the cross-stream direction, the second projection method used eight probes distributed in the y-direction, (see § 3.2). A comparison is made in § 4 of the planar portion of the jet large-scale structure obtained by both projection methods. This comparison confirms the suitability of using only three laterally spaced rakes in conjunction with LSE as the basis for POD mode projection.

The choice of three spanwise oriented rakes was based upon the need to strike a balance between capturing the cross-stream flow with sufficient fidelity (via LSE)

https://doi.org/10.1017/S0022112002008364 Published online by Cambridge University Press

and having sufficient resolution in the spanwise coordinate so that the basic three-dimensional character of the large-scale motions could be resolved without significant distortion due to spatial aliasing.

The LSE technique was applied to reconstruct the velocity field in the y-direction based on instantaneous velocity measurements at the three y' locations listed above for each z-location along the three rakes. Recalling that time and the z-direction are homogeneous coordinates, equation (3.2) can be rewritten as

$$\widetilde{u}_i(y,z,t) = \sum_{y'} A_{ij}(y,y',\Delta z = z - z' = 0, \Delta t = t - t' = 0) u_j(y',z',t'). \tag{3.5}$$

The interpolation matrix $\boldsymbol{A}(y,y')$ was calculated using (3.4),

$$\langle u_i(y,z,t) u_k(y',z,t)\rangle = \sum_{y'} A_{ij}(y,y') \langle u_j(y',z,t) u_k(y',z,t)\rangle. \tag{3.6}$$

The required cross-correlation matrix can be found from the spectral cross-correlation matrix $S(y,y',\Delta z = 0,f)$ (which was measured previously in Part 1) by using an inverse Fourier transformation,

$$\langle u_i(y,z,t) u_k(y',z,t)\rangle = \frac{1}{2\pi} \int_{-\infty}^{\infty} S(y,y',\Delta z = 0,f)\,\mathrm{d}f. \tag{3.7}$$

Since we must restore the velocity field at a finite number of y-locations ($N_y = 8$) the calculation of $\boldsymbol{A}$ via equation (3.5) is reduced to a matrix equation.

The procedure for reconstruction of the POD modes in physical space may be described in the following eight steps:

(i) A spatial Fourier transform in the z-direction is performed in order to compute $\hat{u}_\alpha(y',k_z,t) = FT\{u_\alpha(y',z,t)\}$.

(ii) The Fourier transform in time is calculated, $\widehat{u}_\alpha(y',k_z,f) = FT\{\hat{u}_\alpha(y',k_z,t)\}$.

(iii) Using the LSE method, the velocity field is estimated at all y-locations $\widehat{u}_\alpha(y';k_z,f) \longrightarrow \widetilde{\widehat{u}}_\alpha(y;k_z,f)$ by applying a version of (3.5), converted to the physical–Fourier space, $\widetilde{\widehat{u}}_i(y;k_z,f) = \sum_{y'} A_{ij}(y,y')\widehat{u}_j(y';k_z,f)$. The matrix $\boldsymbol{A}$ is calculated using (3.6) and (3.7).

(iv) Using the orthogonality property of the POD modes, the POD coefficients (in Fourier space) $c^{(n)}(k_z,f)$ can be computed by projecting the POD modes onto an instantaneous realization,

$$c^{(n)}(k_z,f) = \int \widetilde{\widehat{u}}_\alpha(y,k_z,f)\varphi_\alpha^{(n)*}(y;f,k_z)\,\mathrm{d}y. \tag{3.8}$$

(v) The Fourier transform of each POD mode can be restored,

$$\widehat{u}_\alpha^{(n)}(y,k_z,f) = c^{(n)}(k_z,f)\varphi_\alpha^{(n)}(y,f,k_z). \tag{3.9}$$

(vi) An inverse temporal Fourier transform provides the POD mode in a mixed Fourier–physical space,

$$\hat{u}_\alpha^{(n)}(y,k_z,t) = FT^{-1}\{\widehat{u}_\alpha^{(n)}(y,k_z,f)\}. \tag{3.10}$$

(vii) Finally, an inverse spatial Fourier transform restores the POD modes in the physical domain,

$$u_\alpha^{(n)}(y,z,t) = FT^{-1}\{\hat{u}_\alpha^{(n)}(y,k_z,t)\}. \tag{3.11}$$

https://doi.org/10.1017/S0022112002008364 Published online by Cambridge University Press

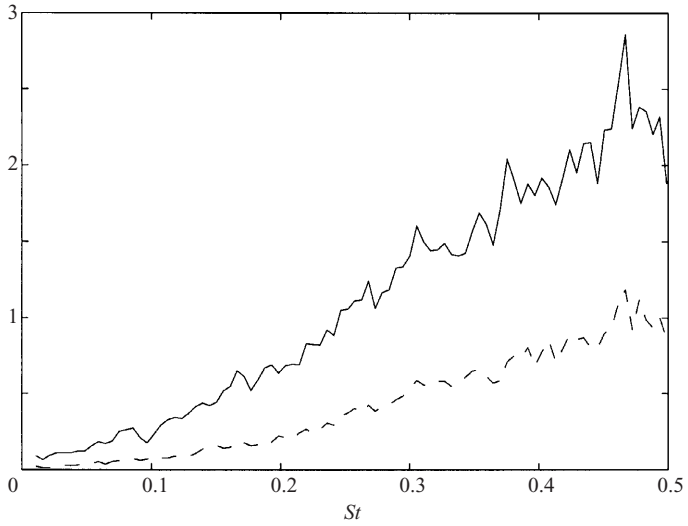


FIGURE 3. Ratio of the norms of phase coefficients ——, $||c_v||/||c_u||$ from (u,v) measurements and – – –, $||c_w||/||c_u||$ from (u,w) measurements for $k_z b/2\pi = 0.5$.

(viii) The fluctuating flow field is then the sum of all POD modes,

$$u_\alpha(y,z,t) = \sum_{n=1}^{\infty} u_\alpha^{(n)}(y,z,t). \tag{3.12}$$

In order to correctly compute the phase coefficients $c^{(n)}$ as described in step (iv) of the reconstruction procedure outlined above, the u-, v-, and w-component velocity fluctuations must be measured simultaneously. Unfortunately, the X-wire is capable of providing only simultaneous (u,v) or (u,w) velocity fluctuation time-series (depending on the X-wire orientation). As noted above, the rake X-wires were oriented in order to obtain (u,v). For the particular case of the planar mode we have $\varphi_w^{(n)} \equiv 0$ so that $c_w^{(n)} \equiv 0$, where

$$c_\alpha^{(n)}(k_z,f) = \int \widetilde{\widehat{u}}_\alpha(y,k_z,f)\varphi_\alpha^{(n)*}(y;f,k_z)\,\mathrm{d}y \quad \text{(no summation on } \alpha). \tag{3.13}$$

Hence, the w-component is not required to restore the planar structure and the simultaneous acquisition of (u,v) time-series from the rakes is completely sufficient. This is not the case for the non-planar modes where the neglect of one of the fluctuating velocity components will result in lost phase information since $c^{(n)} = c_u^{(n)} + c_v^{(n)} + c_w^{(n)}$.

In order to gauge the size of the error associated with the neglect of the w-component, $c_w^{(n)}$ can be computed by acquiring additional (u,w) time-series measurements obtained in the jet. From the two groups of measurements, (u,v) and (u,w), the relative size of $c_u^{(n)}, c_v^{(n)}$ and $c_w^{(n)}$ can be determined and compared. As an example, figure 3 presents phase coefficient modulus ratios $|c_v^{(1)}|/|c_u^{(1)}|$ and $|c_w^{(1)}|/|c_u^{(1)}|$ for the first POD mode as functions of non-dimensional frequency St and for $k_z b/2\pi = 0.5$. For a range of $St = 0 \ldots 0.2$, where the POD eigenvalues are essentially non-zero (see figure 1), $|c_v^{(1)}| < 0.7\,|c_u^{(1)}|$ and $|c_w^{(1)}| < 0.2\,|c_u^{(1)}|$. These results (and others that are not presented here) provide justification for not including the w-component phase coefficient in the reconstruction of the flow structure. In particular, these results suggest

https://doi.org/10.1017/S0022112002008364 Published online by Cambridge University Press

that the neglect of $c_w^{(n)}$ gives rise to only a small error in the reconstruction of the lowest-order non-planar modes. This is related to the dominance of the u-component for non-planar POD modes as described in Part 1.

The triple-rake arrangement was used to record the instantaneous velocity field with sampling frequency f_s for $N_b = 100$ blocks of $N_p = 1024$ points per block. For the conditions under which the jet was operated, conventional power spectra reveal that the frequency bandwidth for the fluctuating velocity extends to approximately 5 kHz. In order to avoid temporal aliasing and to characterize the turbulence satisfactorily, this would dictate a sampling frequency for conventional turbulence measurements of at least 10 kHz. However, since the focus of this experiment is on the large-scale structure in the flow, it was shown in Part 1 that a much lower sampling frequency combined with the use of analogue anti-alias filters offers the best approach. In particular, it was found that the cross-spectral functions which form the experimental input to the POD exhibit little correlation for local non-dimensional frequencies $fb/U_M > 1$. Consequently, the local non-dimensional sampling frequency for the experiments was set at $f_s b/U_M = 8.0$. Using measured mean flow widening and mean velocity decay rates, this gives a streamwise variation of the sampling frequency as $f_s(x/D) = 170\ U_0/D\ (x/D)^{-3/2} = 4.7 \times 10^5 (x/D)^{-3/2}$ (Hz). This corresponds to a sampling frequency of $f_s = 0.8$ kHz at $x/D = 70$. The cutoff frequency of the anti-alias analogue filters was set to $\frac{1}{2} f_s$ in order to prevent temporal aliasing. The total sample time for the instantaneous velocity field records (at $x/D = 70$) is then $T = N_p N_b / f_s = 128$ s.

3.2. *POD mode projection using flow-field realizations from a y-aligned triple rake*

Instantaneous realizations of the flow onto which the POD eigenfunctions are to be projected were also acquired with a y-aligned triple X-wire rake arrangement as shown in figure 4. As indicated, all the rakes are at the same x/D location and are oriented in the cross-stream direction, parallel to each other. The rakes are separated in the spanwise direction by a user-selected distance, H_z. As in the previous implementation, each of the three rakes contains eight X-wire probes, for a total of 48 channels of constant temperature anemometry.

Flow-field realizations from the y-aligned rake were performed in support of the primary experiment described in the previous section. The spatial aliasing of spanwise wavenumber modes is expected to be more significant for instantaneous realizations obtained with the y-aligned rake arrangement. As such, comparison of the planar part of the large-scale structure resulting from projection of the same POD modes onto both realizations allows an assessment of the effect of spanwise aliasing on the resulting large-scale structure topology. In addition, since the y-aligned rakes use more probes in the cross-stream direction, it can also provide a check on the interpolation provided by LSE.

At $x/D = 70$, the y separation between probes in each rake is $\Delta y = \frac{4}{7} b$, which is the same as in the two-rake experiment reported in Part 1. This value was selected based, in part, on a series of supporting single-rake POD measurements involving 16 X-wires equally spaced across the jet. Based upon the results of the single-rake measurements, for the Δy spacing quoted above, spatial aliasing in the y-direction would not be expected to significantly influence the u- or v-modes. The spanwise separation H_z between the rakes was b, which is 2.5 times that used in the z-aligned rake experiment. The corresponding maximum resolved spanwise wavenumber is $k_{z\,\max} b/2\pi = 0.5$. A discussion of issues related to spatial aliasing of spanwise wavenumber modes will be presented in conjunction with the presentation of experimental results in the following

https://doi.org/10.1017/S0022112002008364 Published online by Cambridge University Press

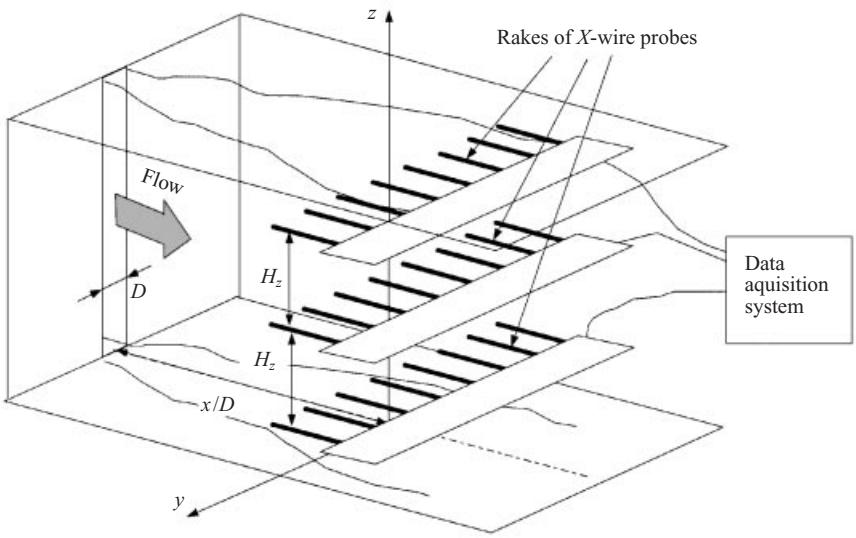


FIGURE 4. The y-aligned triple-rake set-up.

sections. The sampling frequency and anti-alias filter settings were identical to those used in the z-aligned triple-rake experiment.

4. Experimental results

The topology of the turbulent planar jet large-scale structure as obtained from projection of the POD eigenmodes onto instantaneous realizations of the flow is presented in this section. Since the POD eigenmodes and eigenvalues in the turbulent planar jet scale in a self-similar manner, we will present only the flow-field reconstruction obtained at $x/D = 70$ and this may be considered representative of the other locations investigated.

It is common to use a triple decomposition of the velocity field (Hussain 1986; Cantwell 1981) in order to account for the presence of the large-scale flow structure,

$$\boldsymbol{u} = \bar{\boldsymbol{U}} + \boldsymbol{u}_{ls} + \boldsymbol{u}_{fs} \tag{4.1}$$

where $\bar{\boldsymbol{U}}$ is the mean velocity field, $\boldsymbol{u}_{ls}$ represents the large-scale structure and $\boldsymbol{u}_{fs}$ is finer scale, phase incoherent turbulence. In an analogous manner we will represent the resolved flow structure in terms of a summation of the dominant POD modes (i.e. similar in concept to Lumley's 'characteristic eddy'),

$$\boldsymbol{u}_{resolved} = \sum_{n=1}^{N} \boldsymbol{u}^{(n)}. \tag{4.2}$$

Since we are interested only in the large-scale motions in the jet, we neglect $\boldsymbol{u}_{unresolved}$ which are those motions that do not contribute to the cross-spectral tensor $\Phi_{\alpha\beta}(y, y'; f, k_z)$ for the Δy and Δz probe separations used in the experiment described in Part 1. In effect, the probe spacing (particularly in the inhomogeneous coordinate y) sets the range of resolved spatial scales and therefore our definition of the term large-scale structure. The large-scale flow structure is then represented as a series

https://doi.org/10.1017/S0022112002008364 Published online by Cambridge University Press

consisting of the mean flow $\bar{\boldsymbol{U}}(y)$ and N POD modes $\boldsymbol{u}^{(n)}$,

$$\boldsymbol{u}_{struc} = \bar{\boldsymbol{U}}(y) + \sum_{n=1}^{N} \boldsymbol{u}^{(n)}. \tag{4.3}$$

Note that the mean flow is time-independent and is thus orthogonal to the POD modes. From (4.3) it follows that the mean flow can be treated as the dominant POD mode. The remaining POD modes can be viewed as perturbations of the mean flow. For instance, a first approximation of the large-scale flow structure is $\boldsymbol{u}_{struc} = \bar{\boldsymbol{U}}(y) + \boldsymbol{u}^{(1)}$. Based upon the rapid energy convergence of the POD eigenvalues as summarized in figure 20 of Part 1, only the first two POD modes ($N = 2$) were used in (4.3) to obtain the shape of the coherent structure. Further, owing to their dominance in terms of energy content, only the u- and v-component POD modes will be used to reconstruct the jet large-scale structure as described in the previous section. Another motivation for this choice was the observation in Part 1 that higher-order w-component modes probably suffer from spatial aliasing in the y-direction.

Given the geometry of the planar jet flow field and in recognition of the dominance of the planar component $k_z = 0$ shown in the POD eigenvalue spectrum of figure 1, it seems natural to first investigate the topology of the planar portion of the large-scale structure. This is the topic of the next section. Subsequently, less energetic non-planar POD components will be added to the planar portion of the structure in order to investigate the gross three-dimensional character of the large-scale motions. In taking this approach, however, it must be kept in mind that these planar and non-planar parts are complementary aspects of the same underlying large-scale structure.

4.1. *The planar part ($k_z = 0$) of the jet large-scale structure*

4.1.1. *Projection based on z-aligned 3-rake measurements*

Previous studies (e.g. Antonia *et al.* 1983; Thomas & Brehob 1986) have shown that, in the similarity region of the planar jet, the large-scale structure travels with a convective speed in the range of $U_c \approx 0.60 \ldots 0.65 U_M$ which is approximately independent of y for the inner region of the flow $y/b < 1$. In a frame of reference moving downstream at speed U_c, new variables are then defined as $x \to x - U_c t$, $y \to y$, $\boldsymbol{u} \to \boldsymbol{u} - U_c$. One way to visualize the structural topology of the planar mode is to present the velocity vector field $\boldsymbol{u} - U_c$ as a function of lateral position y and the pseudospatial streamwise coordinate $x = -U_c t$. Alternatively, we may present the spatial distribution of the spanwise vorticity component $\omega_z = 1/2(\partial u/\partial y - \partial v/\partial x)$ in the $(-U_c t, y)$-plane. The advantage of using the vorticity is its invariance in the convecting frame of reference. The drawback is the need to calculate derivatives from a velocity field known only at a limited number of points. We will use both approaches to investigate the topology of the planar jet large-scale structure.

First, we present the reconstruction of the planar component of the jet large-scale structure as obtained by the method described in § 3.1.2 (i.e. based on the measurements from the z-aligned 3-rake experiment). Figure 5 presents a vector plot of the first planar POD mode (without the mean flow superimposed) as a function of both lateral position y/b and pseudospatial coordinate $-U_c t/b$. In effect, the vector field shown in figure 5 represents the dominant planar perturbation to the mean flow which is the second term in the expansion (4.3). The pattern shown in figure 5 indicates strong lateral mixing in the jet. Note, in particular, that this first planar POD mode gives rise to well-defined cross-stream sweeping motions, some examples of which can be recognized easily at $x/b = -U_c t/b = -82, -70, -55, -48, -34, -19$

https://doi.org/10.1017/S0022112002008364 Published online by Cambridge University Press

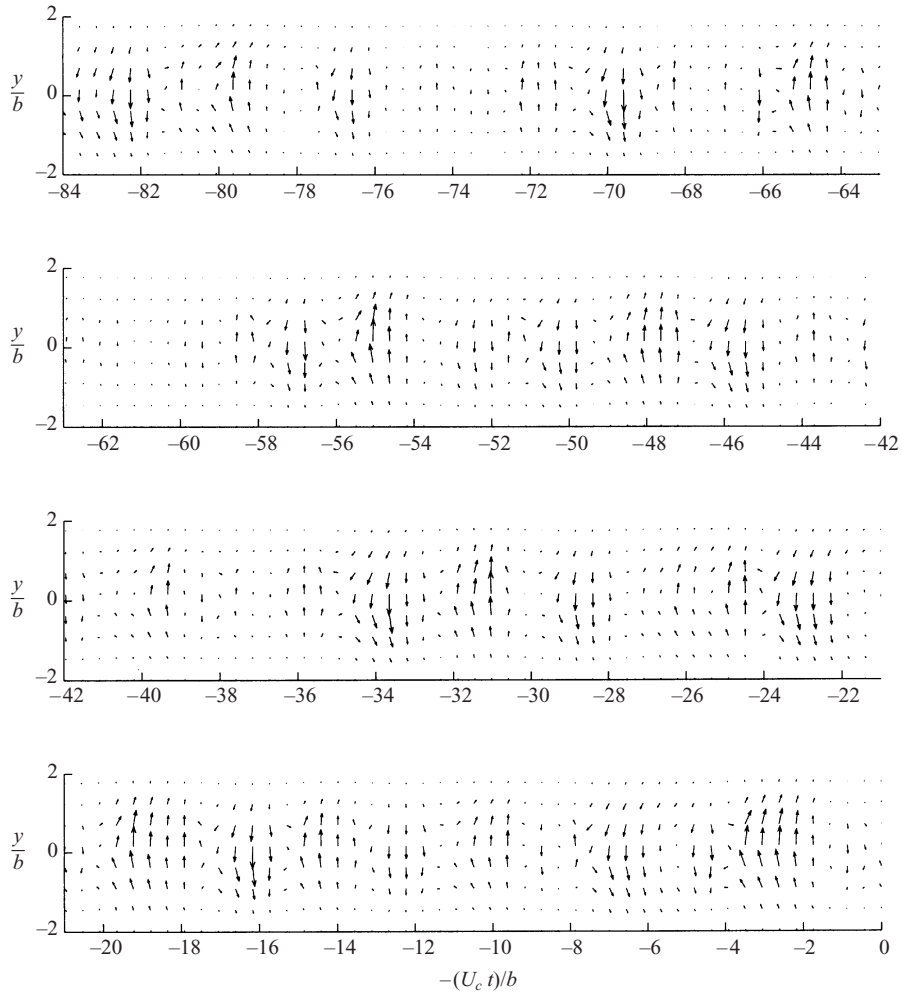


FIGURE 5. Velocity field (u, v) of the reconstructed first planar POD mode $u_\alpha^{(1)}(y, t)$ using the LSE-based projection technique.

and −3. These motions probably account for the comparably large positive values of v-component velocity cross-correlation observed in the turbulent planar jet for even very large lateral probe separations (e.g. Mumford 1982; Antonia *et al.* 1983, Thomas & Brehob 1986; Part 1). Further, the vector field shown in figure 5 is consistent with previous studies which have noted negative correlation between streamwise velocity fluctuations measured simultaneously on opposite sides of the jet centreline. In the past, this has been referred to as the 'jet flapping phenomenon' and was first reported by Goldschmidt & Bradshaw (1973). Figure 5 indicates that this is a manifestation of the planar portion of the large-scale structure.

Since we treat the streamwise coordinate as homogeneous, it is not possible to capture the streamwise evolution of the large-scale structures in the jet. Rather, we are restricted to the examination of local topology at the particular streamwise location of the measurement. Purely for the purpose of visualization of the flow field associated with these local structures, 'pseudostreamlines' are used in addition to velocity vector plots. Remember that the flow field is obtained locally as a function

https://doi.org/10.1017/S0022112002008364 Published online by Cambridge University Press

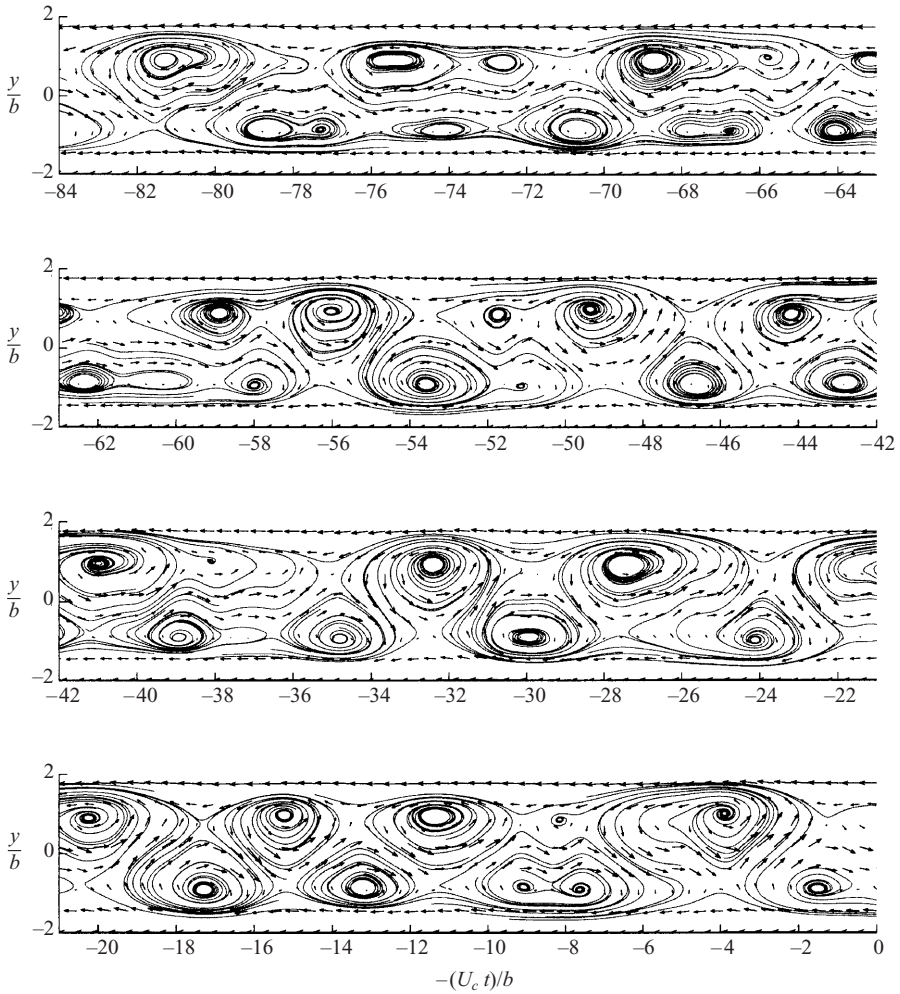


FIGURE 6. The velocity field (u, v) and pseudostreamlines of the reconstructed planar structure $u_\alpha^{planar}(y, t)$ using the LSE-based projection technique with the first $N = 2$ POD modes.

of lateral coordinate y and time t. However, time is treated as equivalent to a spatial coordinate by the assumption that the field is frozen and convected at speed U_c. The resulting flow field in the (x, y)-plane is fitted with these pseudostreamlines in order to help illustrate the structural pattern that convected past the fixed location of observation. Physically, these lines correspond most closely to particle pathlines in the corresponding parallel jet flow. As before, the cross-stream and pseudospatial streamwise coordinates y and x have been non-dimensionalized by the local mean velocity half-width b. Figures 6 and 7 present two sample realizations of the velocity vector field and 'pseudostreamlines' associated with the planar component of the jet large-scale structure in the moving frame of reference obtained by superimposing the mean flow and the first two planar POD modes (i.e. by using (4.3) with $N = 2$ and $k_z = 0$).

The pattern shown in figures 6 and 7 is characterized by a streamwise series of centres and separatrices on both sides of the jet. This clearly indicates the presence of large-scale counter-rotating vortical structures on either side of the jet which are

https://doi.org/10.1017/S0022112002008364 Published online by Cambridge University Press

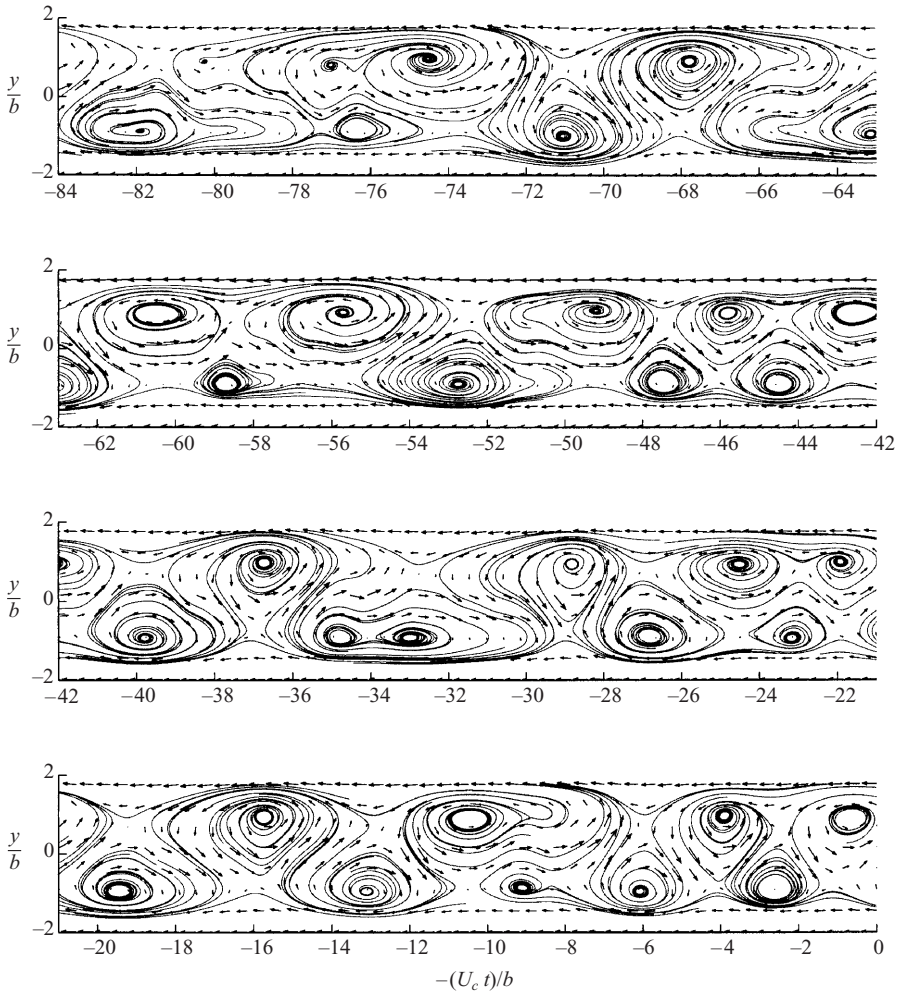


FIGURE 7. The velocity field (u, v) and pseudostreamlines of the reconstructed planar structure $u_\alpha^{planar}(y,t)$ using the LSE-based projection technique with the first $N = 2$ POD modes (another record).

arranged approximately antisymmetrically with respect to the jet centreline. In fact, the structural arrangement closely resembles the classic Kármán vortex street, with the locations of the two vortex lines centred at approximately $y/b \approx \pm 0.85$. There is a strong interaction between structures on opposite sides of the jet in the form of lateral streaming motions that extend well across the flow.

The highly organized structural pattern shown in figures 6 and 7 may seem surprising for the far field of a fully turbulent jet. In general, the presence of small-scale fluctuations makes it difficult to visually extract any information regarding the topology of the underlying large-scale organized motions in turbulent flows. Such small-scale fluctuations quickly diffuse any markers introduced into the flow and make the direct visualization of organized motions virtually impossible. Further, the large-scale structures convect downstream and the introduction of a flow marker such as smoke or dye at stationary point(s) does not necessarily reveal any organized flow pattern because of a mismatch in phase speeds. The clarity of the structural pattern

https://doi.org/10.1017/S0022112002008364 Published online by Cambridge University Press

shown in figures 6 and 7 comes, in part, as a consequence of the fact that POD essentially works as a spatial filter and so the obscuring effect of fine-scale turbulence is effectively removed from the large-scale motions in the jet. In addition, the numerical 'dye markers' that are used in the figures to produce the pseudostreamline patterns are introduced at precisely the correct phase speed. These factors combine to allow us to see clearly the underlying planar structural topology in the jet similarity region.

The structural pattern shown in figures 6 and 7 resembles that envisaged by Oler & Goldschmidt (1982) in their simple kinematic model of the planar jet large-scale structure. In conditional sampling experiments in a heated planar jet, Antonia *et al.* (1986) associated spatially coherent temperature fronts with the separatrix between adjacent structures. Although their conditional measurements were confined to a single side of the flow and were obtained at a single, fixed z location, there is a strong resemblance between certain aspects of figure 6 of their paper and the structural pattern shown in figures 6 and 7.

From an extensive set of results like those shown in figures 6 and 7 statistics related to the planar structural array may be determined. Although there is obviously significant variation in the size of the structures, the typical lateral extent is found to be approximately $1.5b$ while the streamwise extent is about $3.5b/U_c$. This gives a typical lateral to streamwise aspect ratio for the planar structure of approximately $\frac{2}{5}$. The times between the passage of sequential vortices in both of the lines shown in figures 6 and 7 were used to generate a return map which indicated a chaotic distribution of the vortices. Based upon a computed probability distribution function the mean non-dimensional distance between vortices was found to be $U_c\bar{t}/b = 5$. Defining a mean crossing frequency as $\bar{f}_c \equiv 1/\bar{t}$, we obtain $\bar{f}_c b/U_c = 0.12$.

A reconstruction of the planar part of the large-scale structure using the mean flow and only the first planar POD mode, $\bar{\boldsymbol{U}}(y) + \boldsymbol{u}^{(1)}_{resolved}(y, k_z = 0, t)$, is presented in figure 8. Comparison of this representation with that shown in figure 6 at corresponding locations $-U_c t/b$ reveals that, although there are small differences, the overall representation of the planar structure by only the first planar POD mode is good. This is due to the previously demonstrated rapid convergence of the planar POD modes with mode number, particularly for the v-component which plays a very important role in the large-scale structure dynamics. The comparison also suggests an insensitivity of the overall structural topology to higher-order POD modes (as well as the small degree of spatial aliasing).

4.1.2. *POD mode projection based on y-aligned 3-rake measurements*

From the y-aligned 3-rake experiment, the planar component of the large-scale structure can be extracted as well, using the technique described in § 3.1.2, with the third step skipped. In this manner, the first POD planar mode was again reconstructed in physical space and is presented in figure 9. Comparison with figure 5 reveals virtually the same reconstructed modal topology. Small differences are found only for $|y/b| > 1$, where the u-component tends to be more pronounced for the projection based on the y-aligned rakes. This suggests that the LSE interpolation used to restore the velocity field in the z-aligned 3-rake experiment underestimates the u-component velocity fluctuations near the outer portions of the jet. This is a consequence of the rake placement used. In particular, in the z-aligned 3-rake experiment, the rakes were placed in the central portion of the jet. In this region, the v-correlations are maximum, as shown in figure 10 of Part 1. Maximum u-correlations are located near $y/b = 0.7$, as shown in figure 8 of the Part 1. Since LSE interpolation is based on the correlation matrix $R(y, y')$, (§ 3.1.1), it will restore the v-components more faithfully

https://doi.org/10.1017/S0022112002008364 Published online by Cambridge University Press

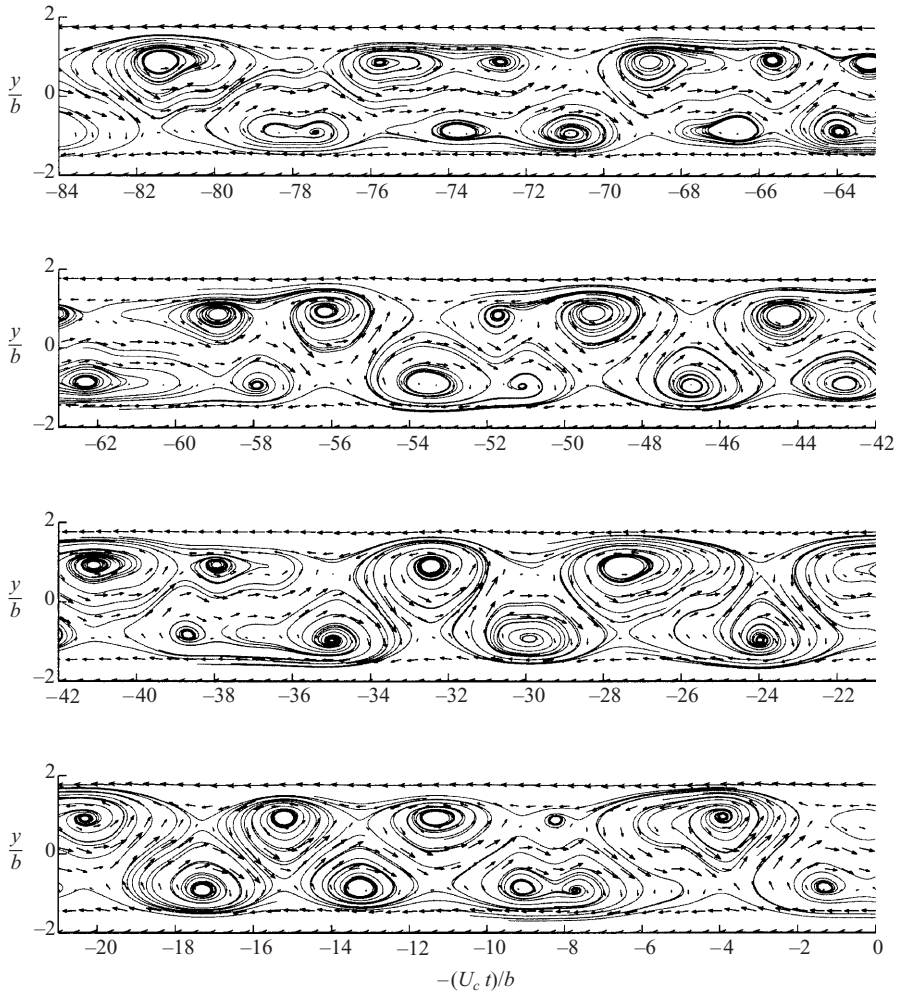


FIGURE 8. The velocity field (u, v) and pseudostreamlines of the reconstructed planar structure $u_\alpha^{planar}(y,t)$ using the LSE-based projection technique with only the first $N = 1$ POD mode.

than the u-component with the rake placement used. In contrast, the y-aligned 3-rake experiment samples both the u- and v-component velocity at 8 positions in the cross-stream direction. However, it is important to point out that the observed differences are small and are not significant enough to alter the essential topology of the planar large-scale structure.

Figure 10 presents both the vector field and superimposed pseudostreamlines for the superposition of the mean flow and first two planar POD modes as reconstructed from the y-aligned 3-rake experiment. As expected, the characteristic topology of the planar component of the large-scale jet structure is very similar to that shown in figures 6 and 7. This further validates the quality of the LSE interpolation in y for the z-aligned rake experiment. In addition, note that the y-aligned 3-rake experiment has a spanwise wavenumber cutoff value $k_z^{\max} b/2\pi = 0.5$ which is 2.5 times smaller than for the z-aligned 3-rake experiment. As such, the spatial aliasing of spanwise wavenumber modes is expected to be much more significant for the y-aligned rake experiment. Despite this, the first POD mode is practically the same

https://doi.org/10.1017/S0022112002008364 Published online by Cambridge University Press

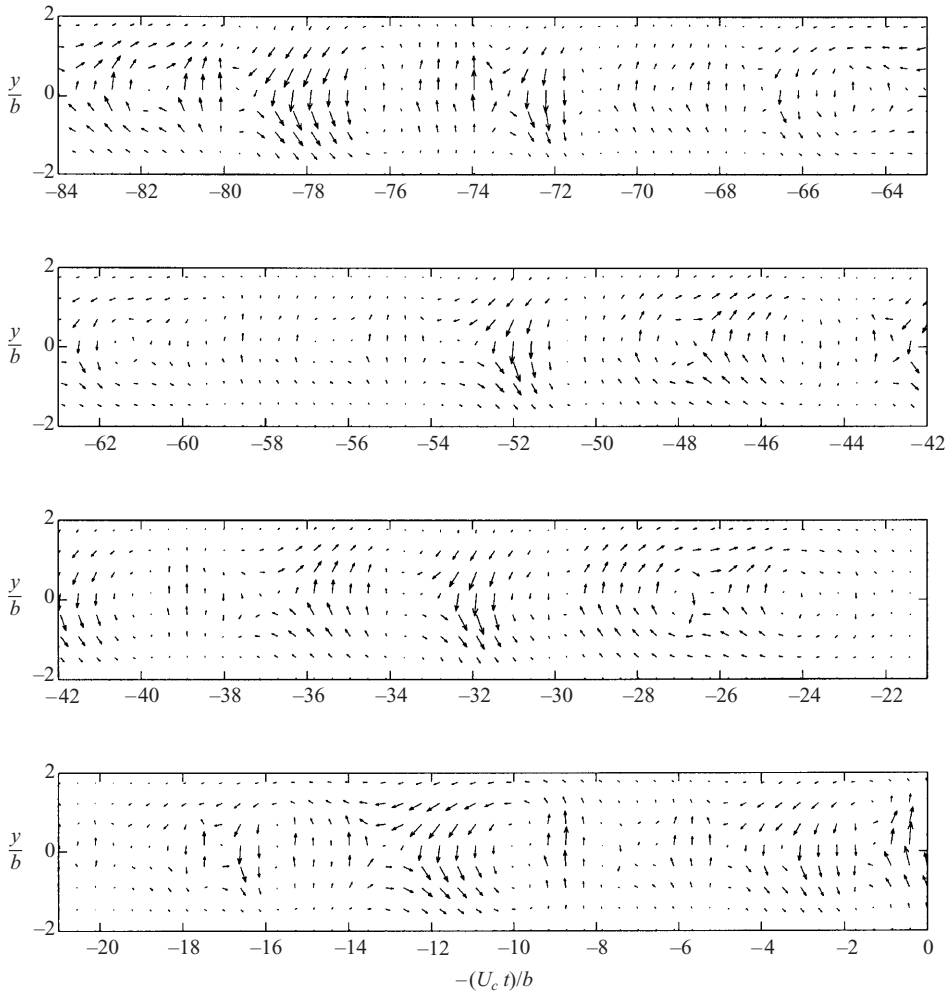


FIGURE 9. Velocity field (u, v) of the reconstructed first planar POD mode $u_\alpha^{(1)}(y,t)$ from the y-aligned rake experiment.

for both experiments. This demonstrates that the aliasing of spanwise wavenumber modes is actually small and the degree of contamination of the leading POD modes does not appear to be topologically significant.

4.1.3. *A comparison of instantaneous flow reconstructions from both experiments*

A quantitative assessment of the ability of the POD to capture the instantaneous dynamics of the planar mode can be made by comparing velocity–time histories at selected cross-stream locations y/b as obtained directly and via the eigenmode projection. In this section, we do this for experiments involving both the y- and z-aligned rakes. Recall that the $\widehat{u}_\alpha(y, k_z = 0, t)$ time series will exhibit small-scale fluctuations that we would not expect the truncated series of the first two planar POD modes to capture. These motions result from the fairly coarse wavenumber resolution of the three-rake arrangement which will fail to reject fully the lowest spanwise wavenumber modes. Thus, a fair procedure would be to compare $\widehat{u}_{POD}(y, k_z = 0, t)$ and $\widehat{v}_{POD}(y, k_z = 0, t)$ based on the two planar POD modes with a suitably temporally

https://doi.org/10.1017/S0022112002008364 Published online by Cambridge University Press

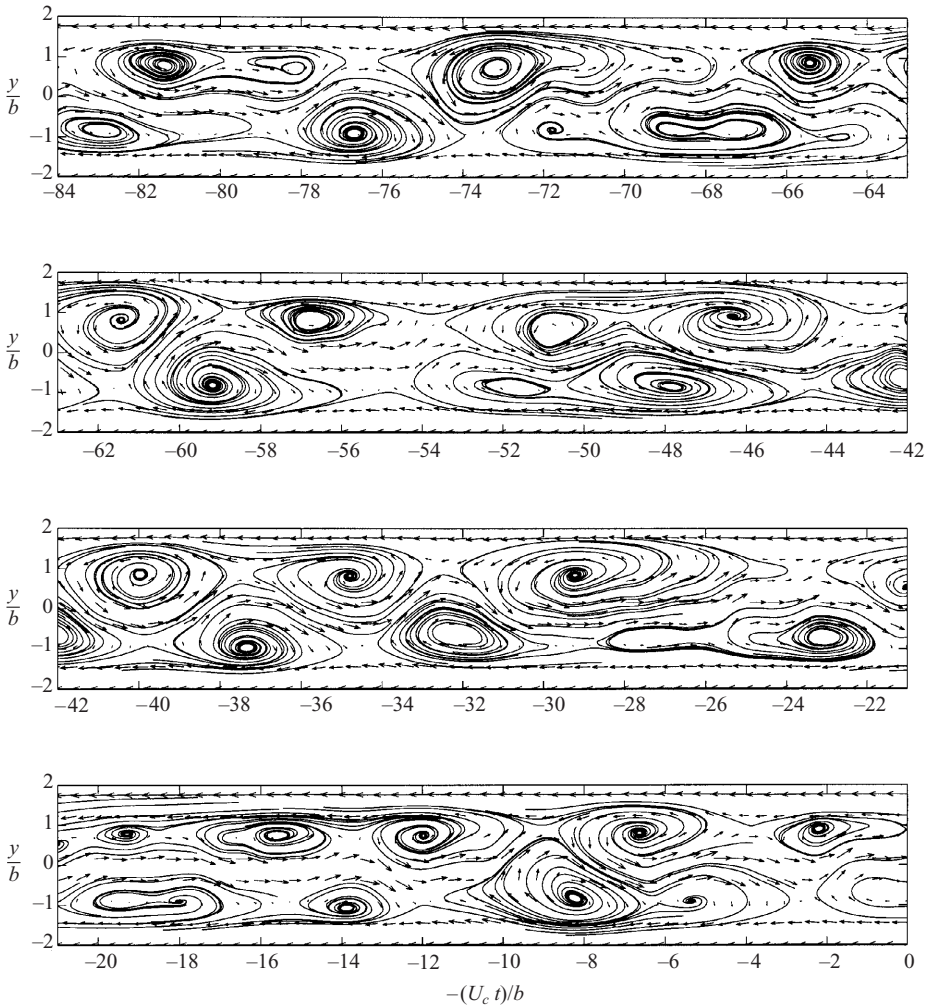


FIGURE 10. The velocity field (u, v) and pseudostreamlines of the reconstructed planar structure $u_\alpha^{planar}(y,t)$ with the first $N = 2$ POD modes from the y-aligned rake experiment.

filtered version of the $\widehat{u}_{\alpha,direct}(y, k_z = 0, t)$ time series obtained directly from the jet. The motivation lies in the recognition that the cross-spectral tensor that forms the experimental input to the POD shows no significant correlation for frequencies $fb/U_m > 0.5$. Hence, it is not reasonable to assume that the planar large-scale structure represented by the POD will involve such high-frequency motions. Recall that the sampling frequency f_s for this experiment was performed at $f_s b/U_m = 8$.

(*a*) *y-aligned 3-rake experiment*

Comparisons of the streamwise and cross-stream velocity component $\widehat{u}_{POD}(y, k_z = 0, t)$ and $\widehat{v}_{POD}(y, k_z = 0, t)$ time series associated with the two planar POD modes extracted from the y-aligned 3-rake experiment and that temporally filtered with cutoff at $f_{cut}b/U_m = 0.5$ are shown in figures 11 and 12, respectively. The heavier curve is the local u- or v-component velocity–time history resulting from the sum of the first two planar POD modes. The lighter curve is a spatially and temporally filtered direct measurement. These figures also show the unfiltered u- and v-component time

https://doi.org/10.1017/S0022112002008364 Published online by Cambridge University Press

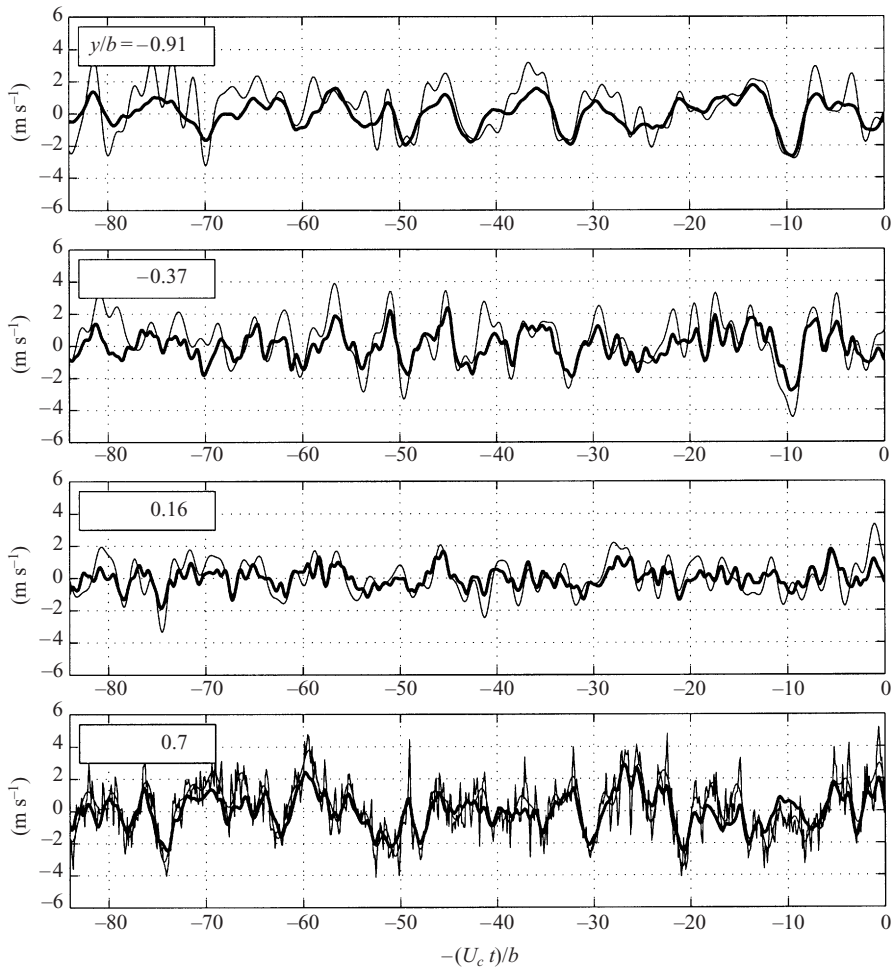


FIGURE 11. Filtered u-component velocity $u_{direct}(y,t)$ (thin line) and the sum of the first two POD modes $u_{POD}(y,t)$ (thick line) for several y-locations from the y-aligned rake experiment. The unfiltered instantaneous velocity $u(y,t)$ is also shown in the $y/b = 0.7$ case for comparison.

series at $y/b = 0.7$ in order to give some idea of the time scales not captured by our implementation of the POD.

The overall agreement between the POD generated and direct time series is observed to be good. When we consider that these measurements are performed in the similarity region of a fully turbulent jet, the ability of just two planar modes to capture much of the instantaneous large-scale variation of $\widehat{u}_{\alpha,direct}(y,k_z=0,t)$ is impressive. One way to quantify the difference in each case is to consider the normalized r.m.s. difference $\{\overline{(\widehat{u}_{\alpha,direct}-\widehat{u}_{\alpha,POD})^2}\}^{1/2}/U_M$. Here, $\widehat{u}_{\alpha,direct}$ and $\widehat{u}_{\alpha,POD}$ denote the large-scale planar velocity fluctuation at fixed y/b as obtained directly and via the superposition of POD modes, respectively, and the overbar denotes temporal averaging. Calculations based on time series like those shown in figures 11 and 12 indicate that the r.m.s. difference varies from 8% for the $\widehat{u}$-component to 5% for the $\widehat{v}$-component. The deviation shown in figures 11 and 12 probably stems from two sources. The first is the relatively poor spatial filter resolution that is associated with the y-aligned triple-rake arrangement of probes. Because of this, a component of the $\widehat{u}$ and $\widehat{v}$ signals

https://doi.org/10.1017/S0022112002008364 Published online by Cambridge University Press

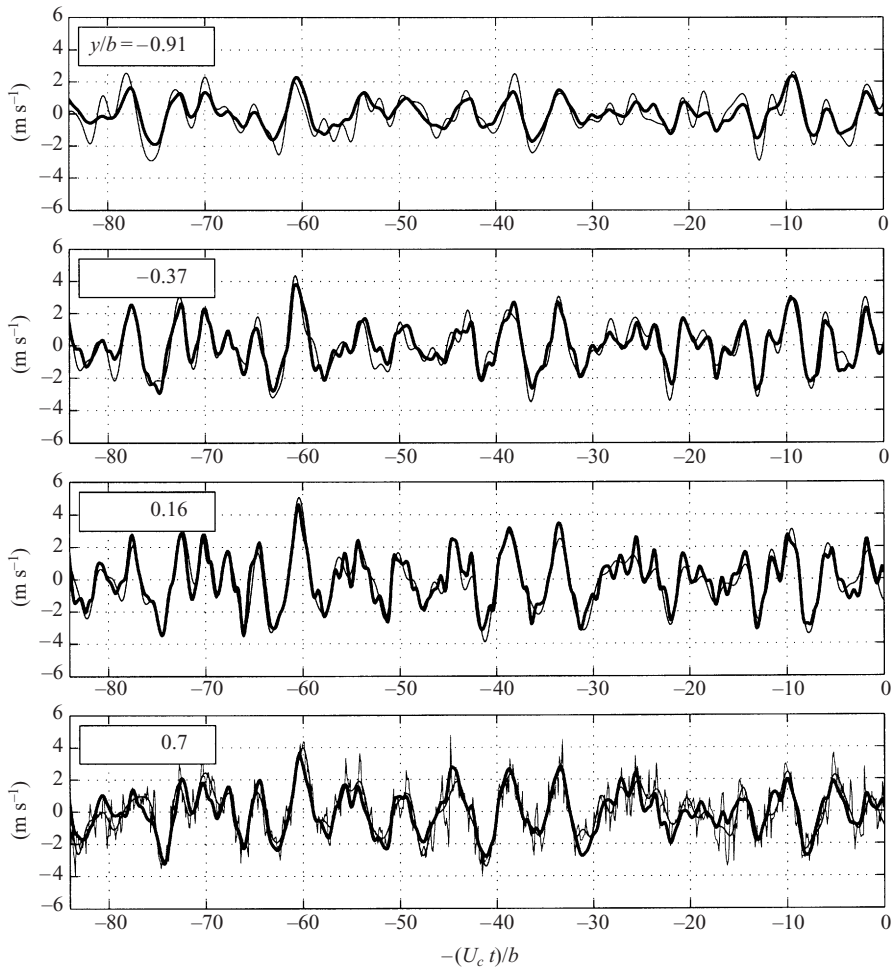


FIGURE 12. Filtered v-component velocity $v_{direct}(y,t)$ (thin line) and the sum of the first two POD modes $v_{POD}(y,t)$ (thick line) for several y-locations from the y-aligned rake experiment. The unfiltered instantaneous velocity $v(y,t)$ is also shown in the $y/b = 0.7$ case for comparison.

shown in figures 11 and 12 is most certainly due to non-planar, but low-wavenumber, modes. In other words, the time series that purports to indicate the planar mode is probably contaminated to some degree by low-wavenumber non planar modes. The second source of error involves the potential mismatch between the instantaneous local flow structure in the jet and the time-averaged structural template (which is the POD eigenmodes). It must be remembered that the POD eigenmodes represent an optimum time-averaged flow structure. Although this structural template is most suitable on average, there can be instances when the local flow structure poorly matches the template and deviations become more significant.

(*b*) *z-aligned 3-rake experiment*

A similar comparison can be made for the z-aligned 3-rake experiment at the three y-locations $y/b = -0.37, 0.16$ and 0.7 with the filtered instantaneous field at the same points. The results are shown at figures 13 and 14 for the u- and v-components, respectively. The notation is similar to that used in figures 11 and 12. While the POD v-component is still reconstructed fairly well, the reconstruction of

https://doi.org/10.1017/S0022112002008364 Published online by Cambridge University Press

the u-components is not as good as before. The difference comes from the fact that the POD reconstruction uses the integral information regarding the velocity field to compute the phase coefficients. As was shown before, the LSE interpolation underestimates the u-component near the edges of the jet and therefore does not predict the u-component correctly. Nevertheless, the LSE procedure still does a good job of recovering most of the essential features, such as the characteristic large-scale v-sweeps of the first POD mode in physical space which turn out to be very significant topologically.

4.2. *Three-dimensional aspects of the jet structure*

In this section, we focus attention on a flow reconstruction that includes several of the dominant non-planar POD modes by using the z-aligned rake experiment. This allows the reconstruction of the gross instantaneous three-dimensional topology of the large-scale structure in the jet. The z-aligned rake experiment provides the opportunity to extract a non-planar component of the POD mode $\widehat{u}_\alpha^{(n)}(y, k_z, t)$. With the Δz probe spacing used for the measurements, the spanwise wavenumber resolution is $\Delta k_z b/2\pi = 0.33$ allowing the resolution of the following spanwise wavenumbers, $k_z b/2\pi = 0.0, 0.33, 0.66$ and 1.0. As shown in the Part 1, above $k_z b/2\pi = 1.0$, there is virtually no energy in the first two POD modes.

As noted earlier, because of the inability of the X-wire probe to measure all three velocity components simultaneously, the flow-field reconstruction was made based on the (u, v) time series only. While this presents no problems for the planar mode, where $\widehat{w}^{(n)}(y, k_z = 0, t) \equiv 0$, in general, this will give the wrong phase coefficient for a non-planar mode, since $c^{(n)} = c_u^{(n)} + c_v^{(n)} + c_w^{(n)}$. However, based on comparison of the relative sizes of $c_u^{(n)}, c_v^{(n)}$ and $c_w^{(n)}$ (as described in § 3.1.2), we find that the neglect of $c_w^{(n)}$ will actually give rise to only a small error in the reconstruction of the non-planar mode. Since we are interested in only the most basic aspects of the jet large-scale structure topology, this small error would hardly alter its principal shape.

By including the non-planar mode, the velocity field corresponding to the large-scale structure is now a function of the three coordinates (y, z, t). We first investigate the flow structure by looking at cross-cuts in the four planes $z/b = 0.2, 0.6$ and $1, 1.4$. In figure 15, the velocity vector field and two-dimensional pseudostreamlines associated with the (u, v)-components are plotted for each plane. For clarity, only every fourth point in the temporal direction is plotted for the velocity vector plots. In addition, the regions of highest spanwise vorticity $|\omega_z| = |\frac{1}{2}(\partial u/\partial y - \partial v/\partial x)| \geqslant 0.3\ U_m/b$ are shown on the same plots as an overlaid shaded region, with light (dark) grey indicating positive (negative) vorticity regions. Comparison of the flow patterns shown in figure 15 reveal an overall similarity which suggests the dominance of the planar part of the structure. On closer inspection, however, some important differences begin to emerge that result from inclusion of the non-planar POD modes. First, the positions of certain vortical structures appear shifted in the different (z/b)-planes. A particular example is labelled $S1$ which shows a distinct 'streamwise' shift with changes in z. Other structures (e.g. $S2$) occur at virtually the same location. This suggests that some of the large-scale spanwise rollers are tilted with respect to the z-axis whereas others are not. Another difference is the apparent strengthening or weakening of the z-directed vorticity associated with certain structures with changes in z. An example is labelled $S3$. This is also consistent with the tilting or bending of structures which will serve redistribute z-directed large-scale vorticity. Hence, figure 15 suggests that while the planar component of the jet large-scale structure is dominant, the non-planar modes give rise to its span-

https://doi.org/10.1017/S0022112002008364 Published online by Cambridge University Press

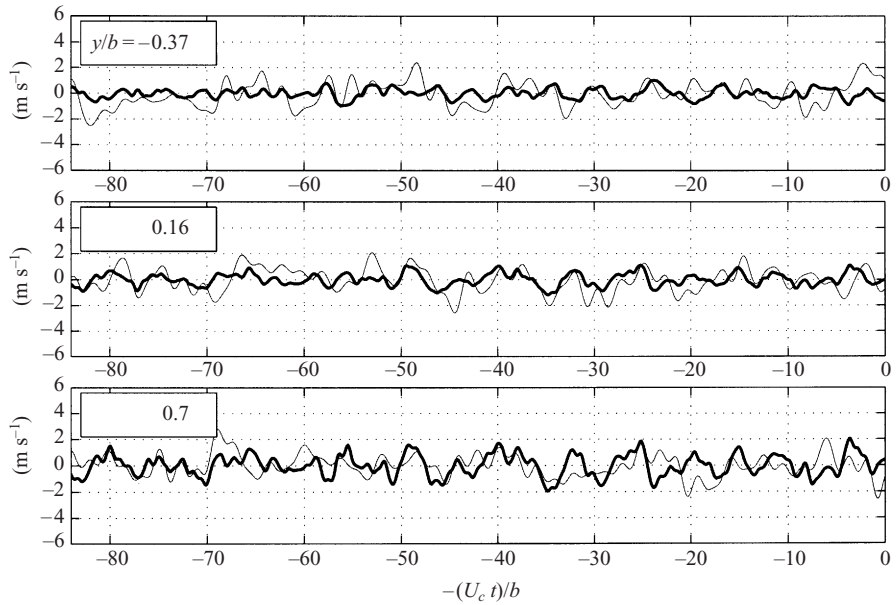


FIGURE 13. Filtered u-component velocity $u_{direct}(y,t)$ (thin line) and the sum of the first two POD modes $u_{POD}(y,t)$ (thick line) for several y-locations from the z-aligned rake experiment.

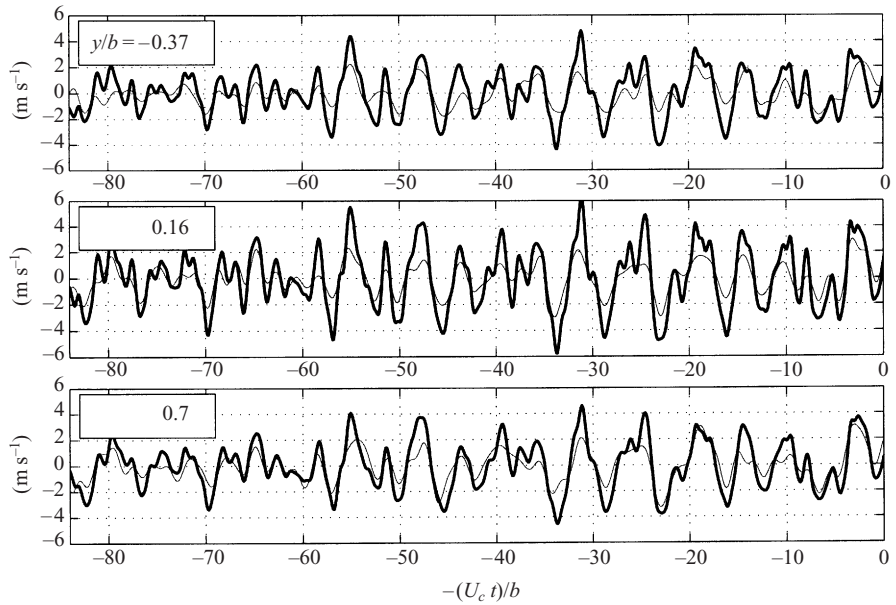


FIGURE 14. Filtered v-component velocity $v_{direct}(y,t)$ (thin line) and the sum of the first two POD modes $v_{POD}(y,t)$ (thick line) for several y-locations from the z-aligned rake experiment.

wise perturbation in the form of bending or tilting. Note also from figure 15 that we can see a strong correlation between the large-scale structures and the regions of highest vorticity concentration. Thus, the spatial distribution of ω_z can provide additional information regarding the spanwise variation of the large-scale structure.

https://doi.org/10.1017/S0022112002008364 Published online by Cambridge University Press

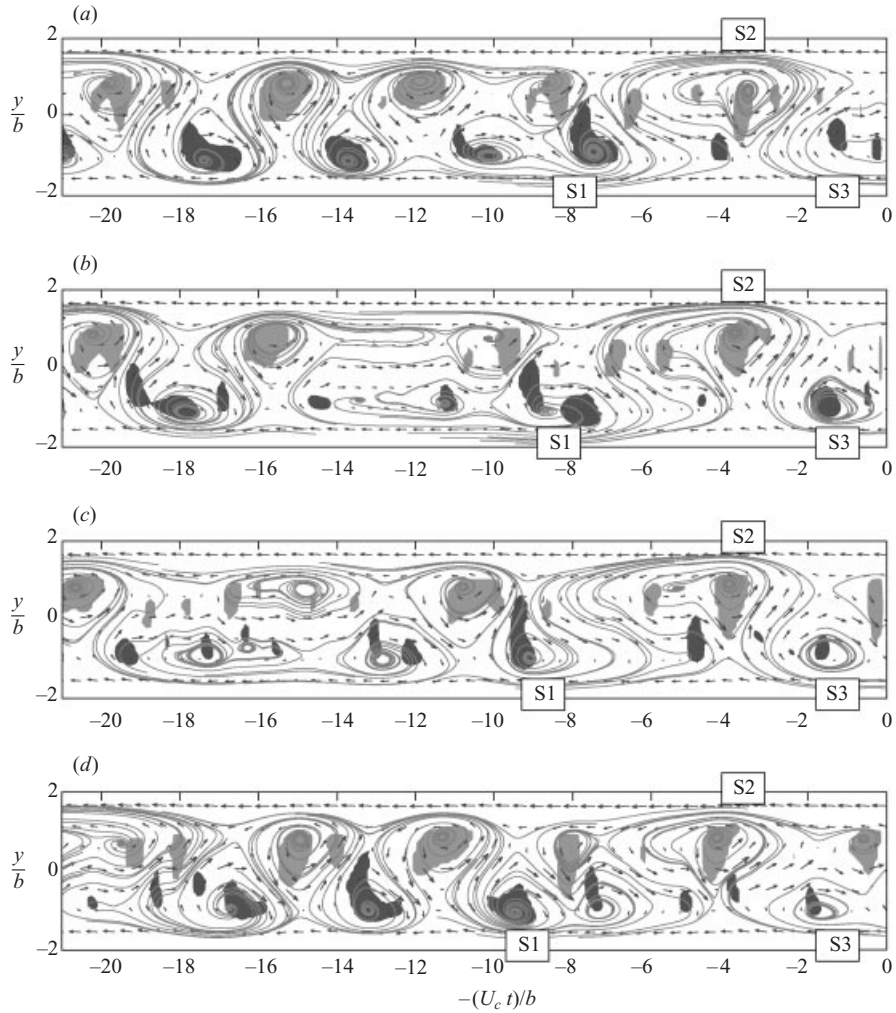


FIGURE 15. The velocity field (u, v) and pseudostreamlines of the reconstructed non-planar coherent structure $u_\alpha^{non\text{-}planar}(y, z, t)$ with the first $N = 2$ POD modes at (*a*) $z/b = 1.4$, (*b*) 1.0, (*c*) 0.6 and (*d*) 0.2 spanwise locations from the z-aligned rake experiment. The regions of high spanwise vorticity $|\omega_z| \geqslant 0.3U_m/b$ are shown as shaded regions, light grey – positive and dark grey – negative.

In order to further investigate the structural topology, the three-dimensional distribution of the z-component of the large-scale structure vorticity $\omega_z = \frac{1}{2}(\partial u/\partial y - \partial v/\partial x) > 0.3U_M/b$ is presented in figure 16. In particular, figure 16 presents iso-surfaces of the z-vorticity component. The regions of highest vorticity are clearly associated with large spanwise roller vortices which bend and tilt by varying degrees in mainly the streamwise direction. The degree of bending varies greatly. In some cases it is slight and in others the structure is strongly bent in the streamwise direction which leads to significant streamwise vorticity. In viewing these structures, it must be remembered that the POD works essentially as a spatial filter and so the small-scale vorticity is effectively removed from the large-scale motions in the jet.

4.3. *Spatial aliasing arising from a single-rake implementation of the POD*

Virtually all previous studies of the large-scale structure in the turbulent planar jet have been based on experiments conducted in a single (x, y)-plane (i.e. at a single

https://doi.org/10.1017/S0022112002008364 Published online by Cambridge University Press

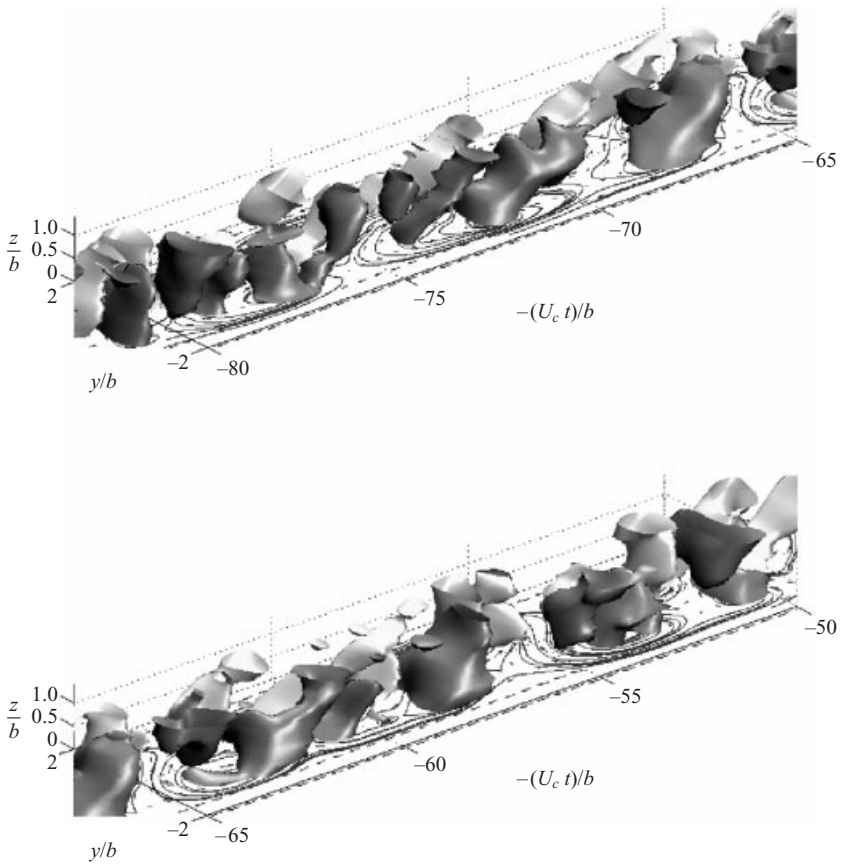


FIGURE 16. Iso-surfaces of ω_z (light grey – positive, dark grey – negative).

fixed spanwise location). Based on the results presented above, we expect that such measurements will be influenced by both the planar flow structure and a weighted sum of aliased non-planar modes. In an attempt to gauge the effect of the non-planar modes on the resulting flow structure, a flow-field reconstruction procedure was performed using POD modes resulting from a single rake of 16 X-wire probes spaced across the jet. Details regarding the single-rake experiment are presented in Part 1. Note that in this implementation the resulting eigenfunctions $\varphi_\alpha^{(n)}(y;f)$ and eigenvalues $\lambda^{(n)}(f)$ no longer explicitly depend on spanwise wavenumber k_z. In a manner analogous to that described previously, these eigenfunctions were projected onto instantaneous flow-field realizations acquired by the single rake. Figure 17 presents both the velocity vector field and 'pseudostreamlines' resulting from the superposition of the mean flow and the first three POD modes as obtained at $x/D = 70$. As before, the cross-stream and pseudo-spatial streamwise coordinates y and x have been non-dimensionalized by the local mean velocity half-width b. Comparison of the flow pattern shown in figure 17 with the planar mode of figure 10 reveals the strong influence of the aliased non-planar modes when measurements are confined to a single $z = const$ plane. In particular, gone is the fairly orderly sequence of centres bounded by separatrices that characterized the planar mode topology. Although figure 17 does suggest the presence of large-scale vortical structures on both sides of the jet, there are now several foci present where streamlines appear

https://doi.org/10.1017/S0022112002008364 Published online by Cambridge University Press

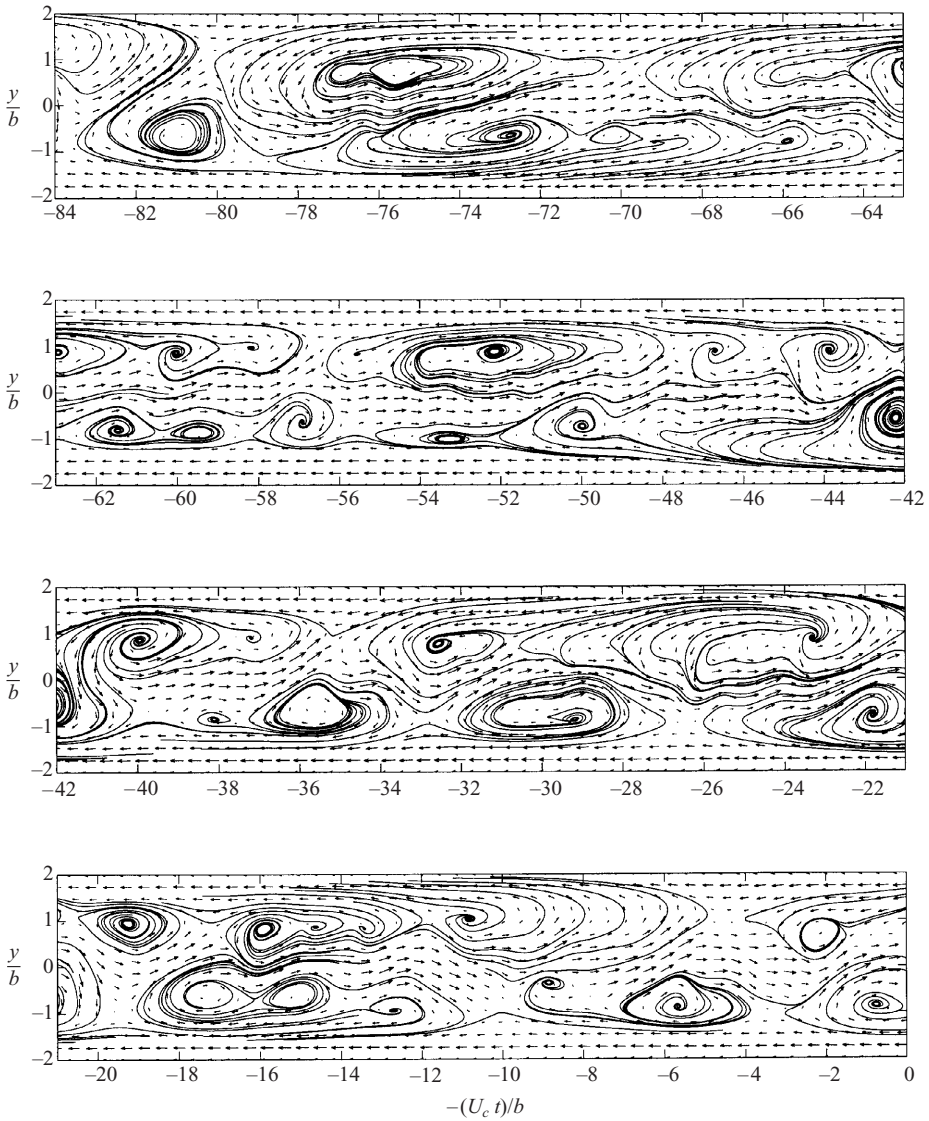


FIGURE 17. The velocity field (u, v) and pseudostreamlines of the reconstructed planar coherent structure $u_\alpha^{planar}(y,t)$ with the first $N = 3$ POD modes from the 16-probe, single-rake experiment.

and disappear. In addition, the overall flow pattern is considerably less organized than that exhibited by the planar mode which is a manifestation of the aliasing of non-planar spanwise modes. This comparison demonstrates the importance of using the spatial filtering provided by the multi-rake arrangements used for the experiments reported above, even in so-called 'planar' turbulent flow fields.

5. Discussion

5.1. *Basic aspects of the planar turbulent jet structural topology*

The experiments show that the dominant large-scale structure in the planar turbulent jet consists of two lines of spanwise vortices centred near $y/b \approx \pm 0.85$ and arranged

https://doi.org/10.1017/S0022112002008364 Published online by Cambridge University Press

approximately asymmetrically with respect to the jet centreline. This planar component of the structure resembles the classic Kármán vortex street and there is a strong interaction between structures on opposite sides of the jet. In particular, the first planar POD mode exhibits strong lateral streaming motions that extend well across the flow. These will certainly be significant in transport and they also give rise to the high v-component cross-correlation coefficients reported by other investigators for even large lateral probe separations. In addition, the first planar POD mode shows that streamwise fluctuations measured simultaneously on both sides of the jet will be correlated negatively on average, thus giving rise to the so-called 'jet flapping' reported in many previous studies. The typical lateral extent of the structures is found to be approximately $1.5b$ while the streamwise extent is $3.5b/U_c$ so that the lateral to streamwise aspect ratio for the planar structure is $\frac{2}{5}$. Comparison of the reconstruction of the large-scale structure using only the mean flow and the first POD mode (as shown in figure 8) with the reconstruction using two POD modes (figure 6) reveals that the principal topology of the large-scale structure remains essentially unchanged. This is due to the importance of the v-component POD mode and its very rapid energy convergence with mode number. In addition, there is also good agreement between the planar topology resulting from both the z- and y-aligned rake experiments which indicates that the aliasing of spanwise wavenumber modes is not sufficient to alter the essential topology of the structures significantly. That is, the overall topology of the planar part of the large-scale structure is robust and is not altered in an essential way by the spatial aliasing of spanwise wavenumber modes. In contrast, however, it was shown that the large-scale structures resulting from a single-rake implementation of the POD are distorted considerably by spanwise aliasing. This calls into question results from any experiment in 'planar' turbulent flows whose measurements are confined to a single cross-span plane.

As demonstrated in Part 1, the large-scale structure that is described in this paper obeys the requirements for global flow similarity. Thus, the results presented at $x/D = 70$ may be considered representative of other streamwise locations investigated. The self-similarity of the structures as well as comparisons with eigenmodes resulting from stability analysis of the base flow presented in Part 1 suggests that they may result from a local instability mechanism of the flow.

In addition to the dominant planar component, the z-aligned three-rake experiment was performed in order to examine the gross three-dimensional character of the flow structure. In particular, it allowed the resolution of three non-planar modes. The results show that the effect of the non-planar mode is to both tilt and bend the spanwise vortex tubes. The bending occurs primarily in the streamwise direction. The degree to which the spanwise vortices are distorted varies. Some vortices are nearly streamwise oriented whereas for others only slight distortion of a primary spanwise vortex is noted.

Although effects of only three non-planar modes were examined, in reality a continuous spectrum of non-planar modes $k_z b/2\pi < 1$ will distort the spanwise vortices. It is expected that the result will be similar in overall topology to that presented in this paper, but will involve finer-scale convolutions of the z-aligned primary vortex tube.

5.2. *On the prospects for modelling the turbulent jet structure*

The rapid energy convergence of the POD modes and the dominance of the first planar component over the non-planar components suggest the possibility of building a realistic low-dimensional model of the planar jet based on the interaction of large-

https://doi.org/10.1017/S0022112002008364 Published online by Cambridge University Press

scale structures. Since the temporal-spatial behaviour of the most energetic structures in the jet was extracted, this provides a rigorous check regarding the validity of model predictions. If the number of equations in the model is reasonably small and can be studied analytically or numerically, comparison of the predicted dynamics with the results of the reconstruction analysis presented here will help in tuning the model parameters and in verifying assumptions inherent in the model.

Of particular relevance regarding model development is to determine what portion of the Reynolds stress is attributable to the large-scale structure and how much is captured by the planar and non-planar POD modes. Before doing this, let us recall that POD reconstruction essentially works as a spatial filter, allowing us to extract the large-scale structure from the obscuring effects of the fine-grain turbulence. The filtering property of the POD is governed by the measurement resolution in the cross-stream and spanwise directions, as well as the sampling frequency which, in a sense, is equivalent to the resolution in the streamwise direction. Obviously, the resolution in each of the three coordinates must be increased if we want to resolve smaller structures in the flow. In Part 1, we presented a detailed discussion regarding spatial resolution issues and the possible aliasing of the POD modes. One of the key results was that the cross-stream resolution used in the experiments was sufficient to resolve only the first four u- and v-component POD modes. For the w-component, only two could be properly resolved. Thus, the ultimate limitation in the ability of the measurement to extract planar large-scale motions in the jet will be governed by the cross-stream separation between probes. There are large-scale anisotropic motions in the jet which are actively involved in Reynolds stress production but which are not captured by the hot-wire array used in this experiment. For example, at $x/D = 70$, the Δy probe spacing is $0.57b$. If the unresolved planar scales have the same streamwise to lateral aspect ratio as the resolved motions (i.e. $\frac{2}{5}$), then the unresolved streamwise length scale is approximately $1.4b$. This gives a characteristic upper frequency limit for the unresolved scales of $fb/U_m \approx 0.5$. From the eigenvalues shown in figure 1, we can see that above this frequency there is no resolved large-scale motion. For this experiment, the term large-scale structure implies the structure with characteristic passage frequencies $St < 0.5$. Above this frequency lie intermediate-scale Reynolds-stress-producing motions that are unresolved by the experiment. In order to estimate the portion of the Reynolds stress accounted for by the resolved scales, spatially and temporally filtered time series from both the instantaneous flow-field realizations and those resulting from projection of the POD modes were used in order to compute the Reynolds-stress variation across the jet. This was done for both the planar and non-planar components of the reconstructed structure. The planar and non-planar parts of the Reynolds stress for the resolved structure (i.e. first two POD modes) were found to contribute approximately 50% of the total Reynolds stress in the jet. It is widely accepted that turbulent shear flows contain large-scale, dynamically significant motions. The values previously quoted would certainly support this. As noted previously, with a finer hot-wire array, more POD modes and the associated Reynolds-stress-producing motion could be resolved. However, there would also be a corresponding increase in the number of required ODEs and model complexity.

A dynamical model is used to compute the temporal evolution of the phase coefficients $c^{(n)}(k_x, k_z; t)$. Thus, the number of required model differential equations is $2 \times N_x \times N_z \times N_m$, where N_x and N_z are the number of the resolved wavenumbers in the streamwise and spanwise directions and N_m is the number of resolved POD modes. The factor of two accounts for the complex nature of the coefficients. More equations would provide more realistic results, but the size and complexity of the

https://doi.org/10.1017/S0022112002008364 Published online by Cambridge University Press

system of ODEs increases dramatically. A real challenge in model development is to retain a minimal number of resolved modes and yet properly account for the unresolved Reynolds-stress-producing motions. Preliminary modelling efforts using only one POD mode with 50 streamwise and 2 spanwise wavenumbers provide encouraging results. The model is found to capture correctly the topology and spatial distribution of the planar jet large-scale structure.

Strictly speaking, the dynamical model of the planar jet would be based on eigenfunctions obtained experimentally at just one Reynolds number, namely $Re = 28000$. Although the set of POD basis functions is complete, it could become non-optimal for flows at different Re. This would narrow the range of applicability of the model. However, we expect viscous effects to appear primarily on the small scales of motion. Investigations of large-scale structures in different turbulent shear flows indicate that the structural topology are macroscale-dependent and are primarily a function of the boundary and initial conditions. For the extracted planar coherent structure presented in this paper, the characteristic Reynolds number can be computed from the r.m.s. velocity averaged across the jet, $u_{rms}^2 = 1/(2b) \int_{-b}^{+b} \overline{u(y,t,z)^2}\, \mathrm{d}y$, and the size $L \sim b$ of the structure, $Re = u_{rms}L/\nu$. For the planar structure at $x/D = 70$, $Re^{planar} \approx 9000$. Consequently, we expect the coherent structure is primarily governed by inertial, rather than viscous forces. Since the model deals with the first few most energetic modes with the rest modelled by a dissipative term, viscous effects will probably not change the spatial shape of the first few POD modes. Rather, it will primarily affect the values of tuning parameters in the model (like the number of involved modes and the energy dissipation rate from the large-scale modes). Hence, it is hoped that for other Reynolds numbers the set of POD modes will still be close to the optimal set and the application of the model can be extended relatively easily for a range of planar turbulent jets with different Re-numbers.

REFERENCES

Adrian, R. J. 1977 On the role of conditional averages in turbulent theory. In *Turbulence in Liquids: Proceedings of the 4th Biennial Symposium on Turbulence in Liquids* (ed. G. Patteson & J. Zakin), pp. 322–332. Science Press, Princeton.

Adrian, R. J. 1979 Conditional eddies in isotropic turbulence. *Phys. Fluids* **22**, 2065–2070.

Adrian, R. J. 1994 Stochastic estimation of conditional structure: a review. *Appl. Sci. Res.* **53**, 291–303.

Adrian, R. J., Jones, B. G., Chung, M. K., Hassan, Y., Nithiandam, C. K. & Tung, A. T. C. 1989 Approximation of turbulent conditional averages by stochastic estimation. *Phys. Fluids* A **1**, 992–998.

Antonia, R. A., Browne, L. W. B., Rajagopalan, S. & Chambers, A. J. 1983 On the organized motion of the turbulent plane jet. *J. Fluid Mech.* **134**, 49–66.

Antonia, R. A., Chambers, A. J., Britz, D. & Browne, L. W. B. 1986 Organized structures in a turbulent plane jet: topology and contribution to momentum and heat transport. *J. Fluid Mech.* **172**, 211–229.

Bendat, J. S. & Piersol, A. G. 1986 *Random Data*, 2nd edn. Wiley Interscience, New York.

Bonnet, J. P., Cole, D. R., Delville, J., Glauser, M. N. & Ukeiley, L. S. 1994 Stochastic estimation and proper orthogonal decomposition: complementary techniques for identifying structure. *Exps. Fluids* **17**, 307–314.

Breteton, G. J. 1982 Stochastic estimation as a statistical tool for approximating turbulent conditional averages. *Phys. Fluids* A **4**, 2046–2054.

Cantwell, B. 1981 Organized motion in turbulent flow. *Annu. Rev. Fluid Mech.* **13**, 457–515.

Cervantes, D. G. & Goldschmidt, V. W. 1981 The apparent flapping motion of a turbulent plane jet – further experimental results. *Trans. ASME* I: *J. Fluids Engng* **103**, 117–126.

Chu, H. C. 1993 An experimental study of nonlinear wave coupling and energy transfer char-

https://doi.org/10.1017/S0022112002008364 Published online by Cambridge University Press

acterizing the transition of a planar jet shear layer. PhD dissertation, University of Notre Dame.

Citriniti, J. H. & George, W. K. 2000 Reconstruction of the global velocity field in the axisymmetric mixing layer utilizing the proper orthogonal decomposition. *J. Fluid Mech.* **418**, 137–166.

Delville, J., Ukeiley, L., Cordier, L., Bonnet, J. P. & Glauser, M. 1999 Examination of large scale structures in a plane mixing layer. Part 1. Proper orthogonal decomposition. *J. Fluid Mech.* **391**, 91–122.

Everitt, K. W. & Robins, A. G. 1978 The development and structure of turbulent plane jets. *J. Fluid Mech.* **88**, 563–583.

Ewing, D. 1995 On multi-point similarity solutions in turbulent free-shear flows. PhD dissertation, SUNY at Buffalo, Amherst, New York.

Glauser, M. N. 1987 Coherent structures in the axisymmetric turbulent jet mixing layer. PhD dissertation, SUNY, Buffalo.

Glauser, M. N. & George, W. K. 1992 Application of multipoint measurements for flow characterization. *Expl Thermal Fluid Sci.* **5**, 617–632.

Goldschmidt, V. W. & Bradshaw, P. 1973 Flapping of a plane jet. *Phys. Fluids* **16**, 354–355.

Gordeyev, S. V. 1999 Investigation of coherent structure in the similarity region of the planar turbulent jet using POD and wavelet analysis. PhD dissertation, University of Notre Dame.

Gordeyev, S. V. & Thomas, F. O. 2000 Coherent structure in the similarity region of the turbulent planar jet. Part 1. Proper orthogonal decomposition eigenmodes and their self-similarity. *J. Fluid Mech.* **414**, 145–194.

Hussain, A. K. M. F. 1986 Coherent structures and turbulence. *J. Fluid Mech.* **173**, 303–356.

Lumley, J. 1967 The structure of inhomogeneous turbulent flows. In *Proceedings of the International Colloquium on the Fine Scale Structure of the Atmosphere and its Influence on Radio Wave Propagation* (ed. A. M. Yaglam & V. I. Tatarsky), pp. 166–178. Doklady Akademii Nauk SSSR, Moscow, Nauka.

Lumley, J. 1970 *Stochastic Tools in Turbulence*. Academic, New York.

Mumford, J. C. 1982 The structure of the large eddies in fully developed turbulent shear flows. Part 1. The plane jet. *J. Fluid Mech.* **118**, 241–268.

Oler, J. W. & Goldschmidt, V. W. 1982 A vortex-street model of the flow in the similarity region of a two-dimensional free turbulent jet. *J. Fluid Mech.* **123**, 523–535.

Papoulis, A. 1984 *Probability, Random Variables and Stochastic Theory*, 2nd edn. McGraw-Hill.

Thomas, F. O. 1991 Structure of mixing layers and jets. *Appl. Mech. Rev.* **44**, 119–153.

Thomas, F. O. & Brehob, E. G. 1986 An investigation of large-scale structure in the similarity region of a two-dimensional turbulent jet. *Phys. Fluids* **29**, 1788–1795.

Townsend, A. A. 1976 *The Structure of Turbulent Shear Flow*. Cambridge University Press.

Ukeiley, L., Cordier, L., Manceau, R., Delville, J., Glauser, M. & Bonnet, J. P. 2001 Examination of large-scale structures in a turbulent plane mixing layer. Part 2. Dynamical systems model. *J. Fluid Mech.* **441**, 67–108.

Ukeiley, L. & Glauser, M. 1995 Dynamics of large-scale structures in a plane turbulent mixing layer. *Rep.* MAE-311. Department of Mechanical and Aeronautical Engineering, Clarkson University.

https://doi.org/10.1017/S0022112002008364 Published online by Cambridge University Press